

Optical phenomena in the field of braneworld Kerr black holes

Jan Schee

*Institute of Physics, Faculty of Philosophy and Science, Silesian University in Opava,
Bezručovo nám. 13, CZ-746 01 Opava, Czech Republic*

schee@email.cz

Zdeněk Stuchlík

*Institute of Physics, Faculty of Philosophy and Science, Silesian University in Opava,
Bezručovo nám. 13, CZ-746 01 Opava, Czech Republic*

Zdenek.Stuchlik@fpf.slu.cz

We study the influence of the tidal charge parameter of the braneworld models onto some optical phenomena in rotating black hole spacetimes. The escape photon cones are determined for special families of locally non-rotating, circular geodetical and radially free falling observers. The silhouette of a rotating black hole, the shape of an equatorial thin accretion disk and time delay effect for direct and indirect images of a radiation hot spot orbiting the black hole are given and classified in terms of the black hole rotational and tidal parameters. It is shown that rising of negatively-valued tidal parameter, with rotational parameter fixed, generally strenghtens the relativistic effects and suppresses the rotation induced asymmetries in the optical phenomena.

Keywords: braneworld; rotating black-hole; optical effects.

1. Introduction

One way of realizing theories describing gravity as a truly higher-dimensional interaction becoming effectively 4D at low-enough energies is represented by the braneworld models, where the observable universe is a 3-brane (domain wall) to which the standard model (non-gravitational) matter fields are confined, while gravity field enters the extra spatial dimensions the size of which may be much larger than the Planck length scale $l_P \sim 10^{-33}$ cm ².

As shown by Randall and Sundrum ³¹, gravity can be localized near the brane at low energies even with a non-compact, infinite size extra dimension with the warped spacetime satisfying the 5D Einstein equations with negative cosmological constant. Then an arbitrary energy-momentum tensor could be allowed on the brane ³⁸.

The Randall-Sundrum model gives 4D Einstein gravity in low energy limit, and the conventional potential of Newtonian gravity appears on the 3-brane with high accuracy ³¹. Significant deviations from the Einstein gravity occur at very high energies, e.g., in the very early universe, and in vicinity of compact objects ^{26,12,18,1}. Gravitational collapse of matter trapped on the brane results in black holes mainly localized on the brane, but their horizon could be extended into the extra dimen-

sion. The high-energy effects produced by the gravitational collapse are disconnected from the outside space by the horizon, but they could have a signature on the brane, influencing properties of black holes²⁶. There are high-energy effects of local character influencing pressure in collapsing matter, and also non-local corrections of “backreaction” character arising from the influence of the Weyl curvature of the bulk space on the brane – the matter on the brane induces Weyl curvature in the bulk which makes influence on the structures on the brane due to the bulk graviton stresses²⁶. The combination of high-energy (local) and bulk stress (non-local) effects alters significantly the matching problem on the brane, compared to the 4D Einstein gravity; for spherical objects, matching no longer leads to a Schwarzschild exterior in general^{26,18}. The Weyl stresses induced by bulk gravitons imply that the matching conditions do not have unique solution on the brane; in fact, knowledge of the 5D Weyl tensor is needed as a minimum condition for uniqueness¹⁸.^a Some solutions for spherically symmetric black holes¹² and uniform density stars¹⁸ have been discussed. It has been shown that in the black hole case the matching conditions could be satisfied and the bulk effects on the black hole spacetimes could be represented by a single “brany” parameter.

Assuming spherically symmetric metric induced on the 3-brane, the constrained effective gravitational field equations on the brane could be solved, giving Reissner-Nordström static black hole solutions endowed with a braneworld parameter b having character of a “tidal” charge, instead of the standard electric charge parameter Q^2 ¹². The tidal charge can be both positive and negative, however, there are some indications that negative tidal charge should properly represent the “backreaction” effects of the bulk space Weyl tensor on the brane¹².

The stationary and axisymmetric solutions describing rotating black holes localized in the Randall-Sundrum braneworld were derived in¹, having the metric tensor of the Kerr-Newman form with a tidal charge describing the 5D correction term generated by the 5D Weyl tensor stresses. The tidal charge has an “electric” character again and arises due to the 5D gravitational coupling between the brane and the bulk, reflected on the brane through the “electric” part of the bulk Weyl tensor¹, in analogy with the spherically symmetric case¹².

When both the tidal and electric charge are present the black hole spacetime structure is much more complex and additional off-diagonal metric components $g_{r\phi}$, g_{rt} are relevant along with the standard $g_{\phi t}$ component, due to the combination of the local bulk effects and the rotational dragging. This distorts the event horizon which becomes a stack of non-uniformly rotating null circles having different radii at fixed θ while going from the equatorial plane to the poles¹. The uniformly rotating horizon is recovered for the rotation parameter a small enough where Kerr-Newman form of the metric tensor is allowed describing charged and slowly rotating black holes¹. In the absence of rotation, the metric tensor reduces to the Reissner-Nordström form with correction term of non-local origin⁹.

^aAt present, no exact 5D solution in the braneworld model is known.

Here we restrict our attention to the Kerr-Newman type of solutions describing the braneworld rotating black holes with no electric charge, since in astrophysically relevant situations the electric charge of the black hole must be exactly zero, or very small²⁹. Then the results obtained in analysing the behaviour of test particles and photons or test fields around the Kerr-Newman black holes could be used assuming both positive and negative values of the braneworld tidal parameter b (used instead of charge parameter Q^2).

The information on the properties of strong gravitational fields in vicinity of compact objects, namely of black holes, is encoded into optical phenomena of different kind that enable us to make estimates of the black hole parameters, including its tidal charge, when predictions of the theoretical models are confronted with the observed data. From this point of view, the spectral profiles of accretion discs around the black holes in galactic binaries, e.g., in microquasars, are most promising^{30,28}, along with profiled spectral lines in the X-ray flux^{25,5,42,21,27,50}. Important information could also be obtained from the quasiperiodic oscillations observed in the X-ray flux of some low-mass black hole binaries of Galactic origin³⁴, some expected intermediate black hole sources³⁹, or those observed in Galactic nuclei^{3,4}. In the case of our Galaxy centre black hole Sgr A*, we could be able to measure the optical phenomena in more detailed form as compared with the other sources, since it is the nearest supermassive black hole with mass estimated to be $\sim 4 \times 10^6 M_\odot$ ¹⁹, enabling to measure the "silhouette" of the black hole and other subtle GR phenomena^{6,10}.

In the present paper, we give an introductory study of the tidal charge influence on the optical phenomena near a rotating black hole. We focus our attention to some characteristic phenomena in close vicinity of the black-hole horizon, where the effects of the tidal charge could be in principle of the same order as those of the black hole mass and spin, contrary to the case of weak lensing effects. The light escape cones are given for families of astrophysically interesting sources, namely in locally non-rotating frames, and frames related to circular geodetical motion and radially free-falling sources in section 4³⁶. The silhouette of the black hole is determined in section 5. Images of the accretion discs are determined in section 6 using the transfer-function method. In Section 7, time delay of hot spot radiation is determined for direct and indirect images assuming circular geodetical motion in close vicinity of the black hole horizon. In Section 8 relevance of some effects is estimated for the Galaxy centre Sgr A* supermassive black hole. Concluding remarks are presented in Section 9.

2. Gravitational field equations on the brane

In the 5D warped space models of Randall and Sundrum, involving a non-compact extra dimension, the gravitational field equations in the bulk can be expressed in the form^{38,12}

$$\tilde{G}_{AB} = \tilde{k}^2[-\tilde{\Lambda}g_{AB} + \delta(\chi)(-\lambda g_{AB} + T_{AB})], \quad (1)$$

where the fundamental 5D Planck mass \tilde{M}_P enters via $\tilde{k}^2 = 8\pi/\tilde{M}_P^3$, λ is the brane tension, and $\tilde{\Lambda}$ is the negative bulk cosmological constant. Denoting $\chi = x^4$ as the fifth dimension coordinate, $\chi = 0$ determines location of the brane in the bulk space, at the point of Z_2 symmetry; $g_{AB} = \tilde{g}_{AB} - n_A n_B$ is the induced metric on the brane, with n_A being the unit vector normal to the brane.

The effective gravitational field equations induced on the brane are determined by the bulk field equations (1), the Gauss - Codazzi equations and the generalised matching Israel conditions with Z_2 -symmetry. They can be expressed as modified standard Einstein's equations containing additional terms reflecting bulk effects onto the brane³⁸

$$G_{\mu\nu} = -\Lambda g_{\mu\nu} + k^2 T_{\mu\nu} + \tilde{k}^2 S_{\mu\nu} - \mathcal{E}_{\mu\nu}, \quad (2)$$

where $k^2 = 8\pi/M_P^2$, with M_P being the braneworld Planck mass. The relations of the energy scales and cosmological constants are given in the form

$$M_P = \sqrt{\frac{3}{4\pi}} \left(\frac{\tilde{M}_P^2}{\sqrt{\lambda}} \right) \tilde{M}_P; \quad \Lambda = \frac{4\pi}{\tilde{M}_P^3} \left[\tilde{\Lambda} + \left(\frac{4\pi}{3\tilde{M}_P^3} \right) \lambda^2 \right]. \quad (3)$$

Local bulk effects on the matter are determined by the “squared energy-momentum” tensor $S_{\mu\nu}$, that reads

$$S_{\mu\nu} = \frac{1}{12} T T_{\mu\nu} - \frac{1}{4} T_\mu^\alpha T_{\nu\alpha} + \frac{1}{24} g_{\mu\nu} (3T^{\alpha\beta} T_{\alpha\beta} - T^2), \quad (4)$$

while the non-local bulk effects are given by the tensor $\mathcal{E}_{\mu\nu}$ representing the bulk Weyl tensor \tilde{C}_{ABCD} projected onto the brane, whereas

$$\mathcal{E}_{AB} = \tilde{C}_{ABCD} n^C n^D. \quad (5)$$

Symmetries of the Weyl tensor imply that $\mathcal{E}_{[AB]} = \mathcal{E}_A^A = 0$ and $\mathcal{E}_{AB} n^B = 0$. Therefore, on the brane, $\chi \rightarrow 0$, there is $\mathcal{E}_{AB} \rightarrow \mathcal{E}_{\mu\nu} \delta_A^\mu \delta_B^\nu$. The $\mathcal{E}_{\mu\nu}$ tensor reflects influence of the non-local gravitational effects in the bulk, including the tidal (“Coulomb”) and transverse traceless (gravitational wave) imprints of the free gravitational field of the bulk.

We restrict our attention to the vacuum (at both bulk and brane) solutions of the gravitational field equations on the brane. Assuming zero cosmological constant on the brane ($\Lambda = 0$) we arrive to the condition

$$\tilde{\Lambda} = -\frac{4\pi\lambda^2}{3\tilde{M}_P^2}. \quad (6)$$

In the absence of matter fields, there is $T_{\mu\nu} = 0 = S_{\mu\nu}$, i.e., we are not interested in the properties of the squared energy-momentum $S_{\mu\nu}$ representing local effects of the bulk. In the vacuum case, the effective gravitational field equations on the brane reduce to the form³⁸

$$R_{\mu\nu} = -\mathcal{E}_{\mu\nu}, \quad R_{\mu}{}^{\mu} = 0 = \mathcal{E}_{\mu}{}^{\mu} \quad (7)$$

implying divergence constraint³⁸

$$\nabla^{\mu} \mathcal{E}_{\mu\nu} = 0 \quad (8)$$

where ∇_{μ} denotes the covariant derivative on the brane.

The equation (8) represents Bianchi identities on the brane, i.e., an integrability condition for the field equations $R_{\mu\nu} = -\mathcal{E}_{\mu\nu}$ ¹. For stationary and axisymmetric (or static, spherically symmetric) solutions Eqs. (7) and (8) form a closed system of equations on the brane.

The 4D general relativity energy-momentum tensor $T_{\mu\nu}$ (with $T_{\mu}{}^{\mu} = 0$) can be formally identified to the bulk Weyl term on the brane due to the correspondence

$$k^2 T_{\mu\nu} \leftrightarrow -\mathcal{E}_{\mu\nu}. \quad (9)$$

The general relativity conservation law $\nabla^{\mu} T_{\mu\nu} = 0$ then corresponds to the constraints equation on the brane (8). This behaviour indicates that Einstein-Maxwell solutions in general relativity should correspond to braneworld vacuum solutions. This was indeed shown in the case of Schwarzschild (R-N)^{26,12} and Kerr (K-N) spacetimes¹. In both of these solutions the influence of the non-local gravitational effects of the bulk on the brane are represented by a single "braneworld" parameter b . The Coulomb-like behaviour in the Newtonian potential

$$\Phi = -\frac{M}{M_P^2 r} + \frac{b}{2r^2} \quad (10)$$

inspired the name tidal charge¹².

3. Null geodesics in Kerr spacetime with a tidal charge

3.1. Geometry

Following the work of¹, and using the standard Boyer-Linquist coordinates (t, r, θ, φ) , we can write the line element of Kerr black-hole (or naked singularity) spacetime on the three-brane in the form

$$\begin{aligned} ds^2 = & -\left(1 - \frac{2Mr - b}{\Sigma}\right) dt^2 + \frac{\Sigma}{\Delta} dr^2 + \Sigma d\theta^2 + \frac{A}{\Sigma} d\varphi^2 \\ & - 2\frac{2Mr - b}{\Sigma} \sin^2 \theta dt d\phi, \end{aligned} \quad (11)$$

6 *Jan Schee and Zdeněk Stuchlík*

where

$$\Sigma = r^2 + a^2 \cos^2 \theta \quad (12)$$

$$\Delta = r^2 - 2Mr + a^2 + b \quad (13)$$

$$A = (r^2 + a^2)^2 - a^2 \Delta \sin^2 \theta. \quad (14)$$

M is the mass parameter, $a = J/M$ is the specific angular momentum and the braneworld parameter b is the *tidal charge* representing imprint of non-local gravitational effects from the bulk space. The metric (11) has the same form as the Kerr-Newman metric, where the tidal charge is replaced by the squared electric charge, Q^2 . The stress tensor on the brane $E_{\mu\nu}$ takes the form ¹

$$E_t{}^t = -E_\varphi{}^\varphi = -\frac{b}{\Sigma^3} [\Sigma - 2(r^2 + a^2)], \quad (15)$$

$$E_r{}^r = -E_\theta{}^\theta = -\frac{b}{\Sigma^2}, \quad (16)$$

$$E_\varphi{}^t = -(r^2 + a^2) \sin^2 \theta, \quad (17)$$

$$E_t{}^\varphi = -\frac{2ba}{\Sigma^3} (r^2 + a^2) \sin^2 \theta \quad (18)$$

that is fully analogical ($b \rightarrow Q^2$) to the components of energy-momentum tensor for Kerr-Newman spacetimes in Einstein's general relativity ¹.

The roots of $\Delta = 0$ identify the type of braneworld Kerr spacetime. There are two possibilities, a black hole or a naked singularity. By introducing $a^2/M^2 \rightarrow a^2$, $b/M^2 \rightarrow b$, $r_+/M \rightarrow r_+$, or putting $M = 1$, we write the roots of $\Delta = 0$ in the form

$$r_+ = 1 + \sqrt{1 - a^2 - b}, \quad (\text{outer horizon}) \quad (19)$$

and

$$r_- = 1 - \sqrt{1 - a^2 - b}, \quad (\text{inner horizon}). \quad (20)$$

The metric given by the line element (11) determines the geometry of rotating black hole in braneworld universe if

$$1 \geq a^2 + b. \quad (21)$$

The strong inequality refers to the case of two horizons r_+ and r_- . For extreme black holes ($1 = a^2 + b$) the horizons coincide $r_+ = r_- = 1$.

It is clear that for $b \geq 0$ the loci of the inner horizon r_- are always positive. But for $b < 0$, the loci of the inner horizon can also be at negative r , as illustrated in Figure 1.

Notice that $a^2 > 1$ is not allowed for standard black holes and for $b > 0$ ²⁹, but such a possibility appears for $b < 0$. The rotational parameter of extreme black

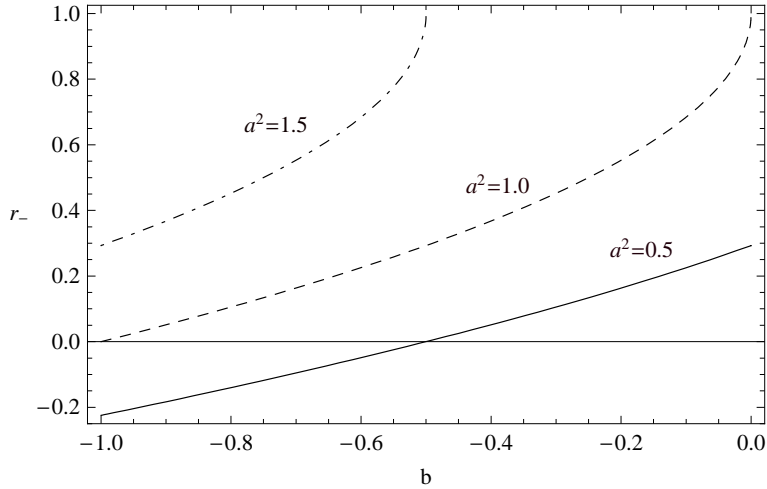


Fig. 1. The plot of the inner horizon radius r_- as a function of tidal charge parameter b for three representative values of rotational parameter $a^2 = 0.5$, $a^2 = 1.0$ and $a^2 = 1.5$.

holes is given by $a^2 = 1 - b$. The case of $1 < a^2 + b$ refers to the braneworld Kerr naked singularities.

In this paper we focus on astrophysically interesting case of black holes, with emitting sources and observers located above the outer horizon.

3.2. Carter's equations

In order to study the optical effects in braneworld Kerr spacetimes, we have to solve equations of motion of photons given by the null geodesics of the spacetime under consideration. The geodesic equation reads

$$\frac{Dk^\mu}{dw} = 0, \quad (22)$$

where $k^\mu = \frac{dx^\mu}{dw}$ is the wave vector tangent to the null geodesic and w is the affine parameter. The normalization condition reads $g_{\mu\nu}k^\mu k^\nu = 0$. Since the components of the metric tensor do not depend on φ and t coordinates, the conjugate momenta

$$k_\varphi = g_{\varphi\nu}k^\nu \equiv \Phi, \quad (23)$$

$$k_t = g_{t\nu}k^\nu \equiv -E, \quad (24)$$

are the integrals of motion. Carter found another integral of motion K as a separation constant when solving Hamilton-Jacobi equation

$$g^{\mu\nu} \frac{\partial S}{\partial x^\mu} \frac{\partial S}{\partial x^\nu} = 0, \quad (25)$$

8 *Jan Schee and Zdeněk Stuchlík*

where he assumed the action S in separated form

$$S = -Et + \Phi\varphi + S_r(r) + S_\theta(\theta). \quad (26)$$

The equations of motion can be integrated and written separately in the form

$$\Sigma \frac{dr}{dw} = \pm \sqrt{R(r)}, \quad (27)$$

$$\Sigma \frac{d\theta}{dw} = \pm \sqrt{W(\theta)}, \quad (28)$$

$$\Sigma \frac{d\varphi}{dw} = -\frac{P_W}{\sin^2 \theta} + \frac{aP_R}{\Delta}, \quad (29)$$

$$\Sigma \frac{dt}{dw} = -aP_W + \frac{(r^2 + a^2)P_R}{\Delta}, \quad (30)$$

where

$$R(r) = P_R^2 - \Delta K, \quad (31)$$

$$W(\theta) = K - \left(\frac{P_w}{\sin \theta} \right)^2, \quad (32)$$

$$P_R(r) = E(r^2 + a^2) - a\Phi, \quad (33)$$

$$P_W(\theta) = aE \sin^2 \theta - \Phi. \quad (34)$$

It is useful to introduce integral of motion Q by the formula

$$Q = K - (E - a\phi)^2. \quad (35)$$

Its relevance comes from the fact that in the case of astrophysically most important motion in the equatorial plane ($\Theta = \pi/2$) there is $Q = 0$.

3.3. Radial and latitudinal motion

The photon motion (with fixed constants of motion E , Φ , Q) is allowed in regions where $R(r; E, \Phi, Q) \geq 0$ and $W(\theta; E, \Phi, Q) \geq 0$. The conditions $R(r; E, \Phi, Q) = 0$ and $W(\theta; E, \Phi, Q) = 0$ determine turning points of the radial and latitudinal motion, respectively, giving boundaries of the region allowed for the motion. Detailed analysis of the θ -motion can be found in ^{8,13}, while the radial motion was analysed (with restrictions implied by the θ -motion) in ⁴¹ and ⁴⁰. Here we extend this analysis to the case of $b < 0$.

The radial and latitudinal Carter equations read

$$\Sigma^2 \left(\frac{dr}{dw'} \right)^2 = [r^2 + a^2 - a\lambda]^2 - \Delta[\mathcal{L} - 2a\lambda + a^2], \quad (36)$$

$$\Sigma^2 \left(\frac{d\theta}{dw'} \right)^2 = \mathcal{L} + a^2 \cos^2 \theta - \frac{\lambda^2}{\sin^2 \theta} \quad (37)$$

where we have introduced impact parameters

$$\lambda = \frac{\Phi}{E}, \quad (38)$$

$$\mathcal{L} = \frac{L}{E^2} = \frac{Q + \Phi^2}{E^2} = q + \lambda^2, \quad (39)$$

and rescaled the affine parameter by $w' = Ew$. We assume $a > 0$.

The reality conditions $(dr/dw')^2 \geq 0$ and $(d\theta/dw')^2 \geq 0$ lead to the restrictions on the impact parameter \mathcal{L}

$$\mathcal{L}_{min} \leq \mathcal{L} \leq \mathcal{L}_{max}, \quad (40)$$

where

$$\mathcal{L}_{max} \equiv \frac{(a\lambda - 2r + b)^2}{\Delta} + r^2 + 2r - b, \quad (41)$$

and

$$\mathcal{L}_{min} \equiv \begin{cases} \lambda^2 & \text{for } |\lambda| \geq a, \\ 2a|\lambda| - a^2 & \text{for } |\lambda| \leq a. \end{cases} \quad (42)$$

The upper(lower) constraint, $\mathcal{L}_{max}(\mathcal{L}_{min})$, comes from the radial-motion (latitudinal-motion) reality condition. The properties of the photon motion are determined by the behaviour of the surface $\mathcal{L}_{max}(r; \lambda, a, b)$, as given by (41). The extrema of the surface \mathcal{L}_{max} (giving spherical photon orbits) are determined by

$$\lambda = \lambda_+ \equiv \frac{r^2 + a^2}{a}, \quad (43)$$

$$\lambda = \lambda_- \equiv \frac{r^2 - br - a^2 - r\Delta}{a(r-1)}. \quad (44)$$

The values of \mathcal{L}_{max} at these extreme points are given by

$$\mathcal{L}_{max}(\lambda_+) \equiv \mathcal{L}_+ = 2r^2 + a^2, \quad (45)$$

$$\mathcal{L}_{max}(\lambda_-) \equiv \mathcal{L}_- = \frac{2r(r^3 - 3r + 4b) + a^2(r+1)^2}{(r-1)^2}. \quad (46)$$

The character of the extrema follows from the sign of $\partial^2 \mathcal{L}_{max} / \partial r^2$. One finds that

$$\frac{\partial^2 \mathcal{L}_{max}}{\partial r^2} = \frac{8r^2}{\Delta}, \quad \text{for } \lambda = \lambda_+, \quad (47)$$

$$\frac{\partial^2 \mathcal{L}_{max}}{\partial r^2} = \frac{8r^2}{\Delta} - \frac{8r}{(r-1)^2}, \quad \text{for } \lambda = \lambda_-. \quad (48)$$

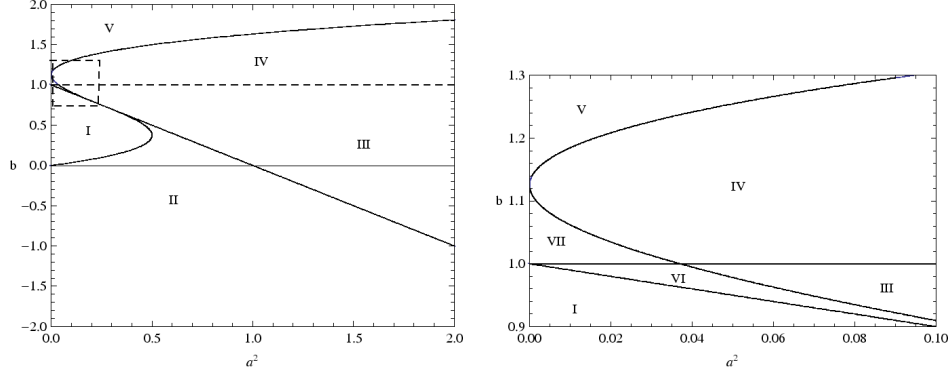


Fig. 2. Left: classification of Kerr spacetime in braneworld universe according to the values of $a^2 + b$, b and n_{ext} (the number of local extrema of the curves λ_{\pm} , which is also the number of circular photon orbits in the equatorial plane). The classification regions are: I) for $a^2 + b \leq 1$ and $n_{ext} = 2$, II) for $a^2 + b \leq 1$ and $n_{ext} = 4$, III) $a^2 + b > 1$ and $b < 1$ and $n_{ext} = 2$, IV) for $a^2 + b > 1$ and $b > 1$ and $n_{ext} = 2$, V) for $a^2 + b > 1$ and $b > 1$ and $n_{ext} = 0$, VI) for $a^2 + b > 1$ and $b < 1$ and $n_{ext} = 4$, VII) for $a^2 + b > 1$ and $b > 1$ and $n_{ext} = 4$. Right: zoom of the area in the dashed rectangle of the left plot, to cover regions VI and VII.

Clearly, there are only minima of \mathcal{L}_{max} along for $\lambda = \lambda_+$, corresponding to unstable spherical orbits.

Further, we have to determine where the restrictions given by the latitudinal motion \mathcal{L}_{min} meet the restrictions on the radial motion \mathcal{L}_{max} . We find that $\mathcal{L}_{max} = \lambda^2$ (for $|\lambda| \geq a$) is fulfilled where

$$\lambda = \tilde{\lambda}_{\pm} \equiv \frac{a(b - 2r \pm r^2 \sqrt{\Delta})}{r^2 - 2r + b}, \quad (49)$$

while $\mathcal{L}_{max} = 2a|\lambda| - a^2$ (for $|\lambda| < a$) is fulfilled where

$$\lambda = \bar{\lambda} \equiv \frac{1}{\Delta} [4r - r^2 - 2b - a^2 + 2\sqrt{\Delta(b - 2r)}]. \quad (50)$$

The extreme points of curves $\tilde{\lambda}_{\pm}$, which are also the intersection points of these curves with λ_- , are determined by the equation

$$f(r; a, b) \equiv r^4 - 6r^3 + (9 + 4b)r^2 - 4(3b + a^2)r + 4b(b + a^2) = 0. \quad (51)$$

The equation $f(r; a, b) = 0$ determines loci of the photon equatorial circular orbits; in an implicit form the radii are given by the condition

$$a^2 = a_{ph\pm}^2(r; b) = \frac{r^2(r - 3)^2 + 4b(r^2 - 3r + b)}{4(r - b)}. \quad (52)$$

The maxima of the curve $\bar{\lambda}$, which also determine the intersections of curves $\bar{\lambda}$ and λ_- are located on r satisfying the equation

$$2r^3 - (3 + b)r^2 + 2br + a^2 = 0. \quad (53)$$

The braneworld Kerr spacetimes can be classified due to the properties of the photon motion as determined by the behaviour of the functions λ_{\pm} , $\tilde{\lambda}_{\pm}$, $\bar{\lambda}$. The classification is governed by their divergences (i.e., by existence of the horizons) and the number of local extrema determining equatorial photon circular orbits n_{ex} . There exist seven classes of the braneworld Kerr spacetimes, with the criteria of separation being $a^2 + b \lesssim 1$, $b \gtrsim 1$ and n_{ex} . The classification is represented in Figure 2. There are two different classes of the black-hole spacetimes, differing by the presence of the photon circular orbits under the inner horizon. However, in the astrophysically relevant region outside the outer horizon, both the classes are of the same character, having two unstable equatorial photon circular orbits, one corotating (at r_{ph1}) and the other counter-rotating (at $r_{ph2} > r_{ph1}$). The tidal charge b introduces no qualitatively new feature into the behaviour of photon motion in the Kerr spacetimes, but the quantitative impact of $b < 0$ with high magnitude are quite relevant, as shown in next sections. All the braneworld Kerr black holes with tidal charge $b < 0$ belong to the class II discussed in the case of standard Kerr-Newman spacetimes⁴⁰. We illustrate in Figures 3-5 functions λ_{\pm} , $\tilde{\lambda}_{\pm}$ and $\bar{\lambda}$ for such a black hole spacetime with parameters $a = 0.9$ and $b = -1.0$. In this case typical for braneworld Kerr black hole with $b < 0$ there exist ten significant values of λ as given in Figures 3 - 5.

For each interval of λ as determined by the sequence of $\lambda_A - \lambda_J$ introduced in Figure 3, there exists a characteristic type of behaviour of the restricting "radial" function \mathcal{L}_{max} and its relation to the "latitudinal" restricting function \mathcal{L}_{min} . They can be found in⁴⁰ and will not be repeated here.

The allowed values of the impact parameter \mathcal{L} lie between the limiting functions \mathcal{L}_{min} and \mathcal{L}_{max} . If the minimum $\mathcal{L}_{max}^{min} \equiv \mathcal{L}_{max}(r_{min}, \lambda_0)$ of the limiting function \mathcal{L}_{max} is less than the value of the limiting function \mathcal{L}_{min} , an incoming photon ($k^r < 0$) travelling from infinity will return back for all values of $\mathcal{L}_0 \in [\mathcal{L}_{min}; \mathcal{L}_{max}]$. If $\mathcal{L}_{max}^{min} > \mathcal{L}_{min}$, the incoming photon ($k^r < 0$) travelling from infinity returns back if its impact parameter \mathcal{L}_0 satisfies the condition $\mathcal{L}_0 \geq \mathcal{L}_{max}^{min}$ and is captured by the black hole if $\mathcal{L}_0 < \mathcal{L}_{max}^{min}$. The minimum \mathcal{L}_{max}^{min} determines (with the particular value of λ) a photon spherical orbit, i.e., a sphere where photons move with $r = const$ but with varying latitude θ (and, of course, varying φ). When the condition $\mathcal{L}_0 = \mathcal{L}_{min}$ is satisfied simultaneously, the spherical photon orbit is transformed to an equatorial photon circular orbit. Photons with $\mathcal{L}_0 = \mathcal{L}_{max}^{min}$ coming from distant regions or regions close to the black hole horizon will wind up around the photon sphere.

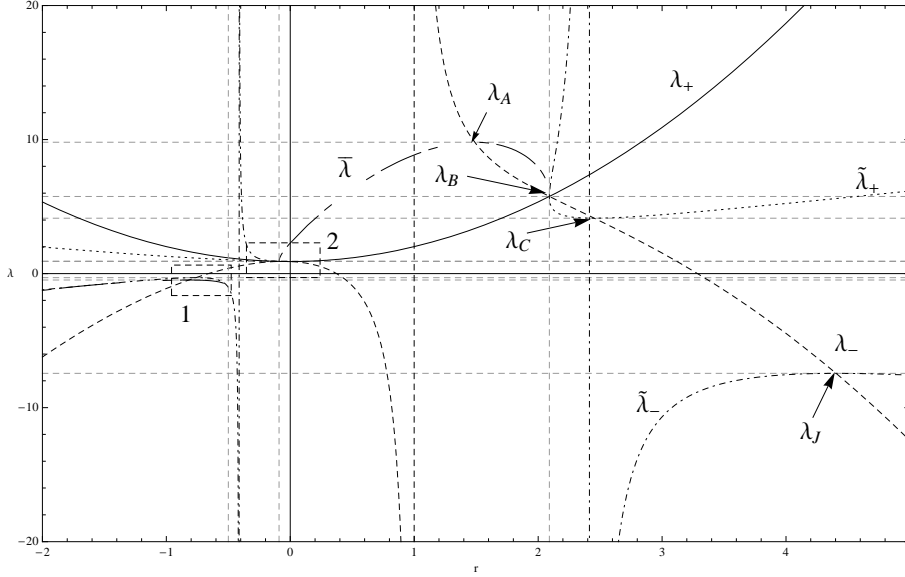


Fig. 3. The graphs of the λ_{\pm} , $\tilde{\lambda}_{\pm}$ and $\bar{\lambda}$ functions are plotted for representative values of the parameters $a = 0.9$ and $b = -1.0$. The two dashed rectangle areas labeled with numbers 1 and 2 are zoomed in the following figures. The horizontal gray dashed lines represent special values of the impact parameter λ , denoted according to the text as $\lambda_A \dots \lambda_J$.

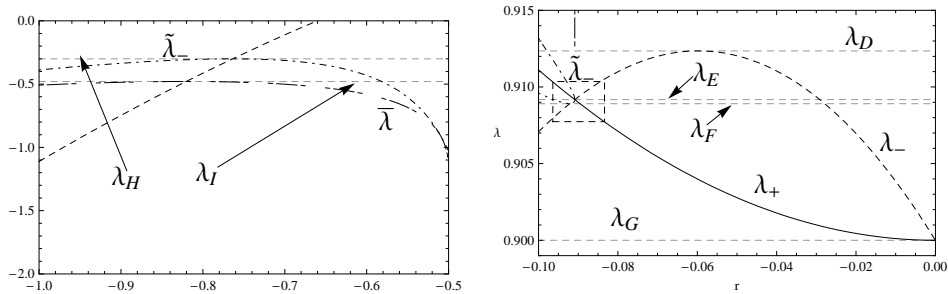


Fig. 4. Left figure is the zoom of dashed area labelled 1 in previous figure. Right figure is the zoom of dashed area labelled 2 in previous figure. The dashed rectangle area here is zoomed in the next figure.

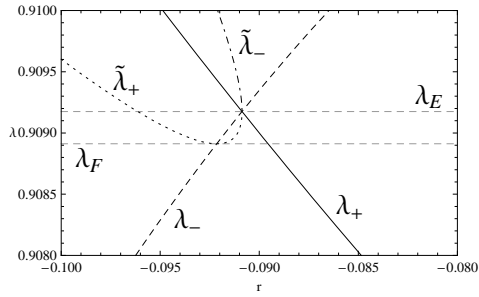


Fig. 5. The zoom of the dashed rectangle area in previous figure.

4. Light escape cones

The optical phenomena related to accretion processes in the field of rotating black holes could be efficiently studied by using the notion of light escape cones of local observers (sources) that determine which portion of radiation emitted by a source could escape to infinity and, complementary, which portion is trapped by the black hole³⁶. Here we focus our attention to four families of observers (sources) that are of direct physical relevance.

4.1. Local frames of stationary and free-falling observers

We consider three families of stationary frames, namely *LNR*F (Locally Nonrotating Frame), *SF* (Static Frame) and *GF*_± (Circular Geodesic Frame) and one non-stationary frame, namely *RFF* (Radially Falling Frame). The *LNR*F are of highest physical importance since the physical phenomena take the simplest form when expressed in such frames, because the rotational spacetime effects are maximally suppressed there^{6,29}. The *GF*_± are directly related to Keplerian accretion discs in the equatorial plane of the spacetime, both corotating and counterrotating, while *RFF* are related to free-falling spherical accretion. The *SF* are fixed relative to distant observers. The *GF*_± and *RFF* are geodetical frames, while *SF* and *LNR*F are generally accelerated frames.

The radial and latitudinal 1-forms of the three stationary frame tetrads are common for all three stationary cases and read

$$\omega^{(r)} = \left\{ 0, \sqrt{\Sigma/\Delta}, 0, 0 \right\}, \quad (54)$$

$$\omega^{(\theta)} = \left\{ 0, 0, \sqrt{\Sigma}, 0 \right\}. \quad (55)$$

*LNR*F correspond to observers with $\Phi = 0$ (zero angular momentum observers). Their time and azimuthal 1-forms read

$$\omega^{(t)} = \left\{ \sqrt{\frac{\Delta\Sigma}{A}}, 0, 0, 0 \right\}, \quad (56)$$

$$\omega^{(\varphi)} = \left\{ -\Omega_{LNR}F \sqrt{\frac{A}{\Sigma}} \sin \theta, 0, 0, \sqrt{\frac{A}{\Sigma}} \sin \theta \right\}. \quad (57)$$

where

$$\Omega_{LNR}F = \frac{a(2Mr - b)}{A} \quad (58)$$

is the angular velocity of *LNR*F as seen by observers at infinity.

The tetrad of *SF* corresponding to observers with $\Omega = 0$, i.e. static relative to observers at infinity, is given by the formulae

$$\omega^{(t)} = \left\{ \sqrt{1 - \frac{2r-b}{\Sigma}}, 0, 0, \frac{a(2r-b)\sin^2\theta}{\sqrt{\Sigma^2 - (2r-b)\Sigma}} \right\}, \quad (59)$$

$$\omega^{(\varphi)} = \left\{ 0, 0, 0, \sqrt{\frac{\Delta\Sigma}{\Sigma - (2r-b)}} \sin\theta \right\}. \quad (60)$$

The GF_{\pm} observers move along φ -direction in the equatorial plane with velocity $V_{GF_{\pm}}$ (+...corotating, -...counterrotating) relative to the $LNRF$ and with angular velocity Ω relative to the static observers at infinity given by [SK]

$$\Omega_{\pm} = \pm \frac{\sqrt{r-b}}{r^2 \pm a\sqrt{r-b}}. \quad (61)$$

The velocity $V_{GF_{\pm}}$ is given by

$$V_{GF_{\pm}} = \pm \frac{(r^2 + a^2)Y \mp a(2r-b)}{\sqrt{\Delta}(r^2 \pm aY)}. \quad (62)$$

where $Y = \sqrt{r-b}$. The standard Lorentz transformation of the $LNRF$ tetrad gives the tetrad of GF_{\pm} in the form

$$\omega_{\pm}^{(t)} = \left\{ \frac{r^2 - 2r + b \pm aY}{Z_{\pm}}, 0, 0, \mp \frac{(r^2 + a^2)Y \mp a(2r-b)}{Z_{\pm}} \right\}, \quad (63)$$

$$\omega_{\pm}^{(\varphi)} = \left\{ \mp \frac{\sqrt{\Delta}Y}{Z_{\pm}}, 0, 0, \frac{\sqrt{\Delta}(r^2 \pm aY)}{Z_{\pm}} \right\}, \quad (64)$$

where

$$Z_{\pm} = r\sqrt{r^2 - 3r + 2b \pm 2aY}. \quad (65)$$

Note that the GF_{\pm} family is restricted to the equatorial plane, while $LNRF$ are defined at any θ .

The RF_{\pm} observers have velocity

$$V_{RF_{\pm}} = \{V^{(r)}, V^{(\theta)}, V^{(\varphi)}\} \quad (66)$$

as measured in $LNRF$. The radially free-falling (or free-escaping) observers starting (finishing) at infinity move with $\theta = \text{const}$. Using the results of ⁴³, we find the velocity components of the free-falling frames in the $LNRF$ frames

$$V^{(r)} = \pm \sqrt{1 - \frac{\Sigma\Delta}{A}}, \quad (67)$$

$$V^{(\theta)} = 0, \quad (68)$$

$$V^{(\varphi)} = 0. \quad (69)$$

Clearly, the free-falling (free-escaping) observers move only radially in the $LNR\dot{F}$, in analogy to particles radially moving in static frames of the Schwarzschild spacetimes. For the radially free-falling sources, the tetrad components $\omega^{(\theta)}$ and $\omega^{(\varphi)}$ coincide with those of the $LNR\dot{F}$ tetrad, while $\omega^{(t)}$ and $\omega^{(r)}$ are transformed. The local Lorentz transformation of the $LNR\dot{F}$ to the RFF_{\pm} tetrad yields

$$\omega_{\pm}^{(t)} = \left\{ \gamma \frac{\Delta \Sigma}{A}, \mp \sqrt{\frac{\Sigma}{\Delta}} V, 0, 0 \right\}, \quad (70)$$

$$\omega_{\pm}^{(r)} = \left\{ \mp \gamma \sqrt{\frac{\Delta \Sigma}{A}} V, \sqrt{\frac{\Sigma}{\Delta}} \gamma, 0, 0 \right\}, \quad (71)$$

$$\omega_{\pm}^{(\theta)} = \{0, 0, \sqrt{\Sigma}, 0\}, \quad (72)$$

$$\omega_{\pm}^{(\varphi)} = \left\{ -\Omega_{LNR\dot{F}} \sqrt{\frac{A}{\Sigma}} \sin \theta, 0, 0, \sqrt{\frac{A}{\Sigma}} \sin \theta \right\}. \quad (73)$$

4.2. Construction of escape cones

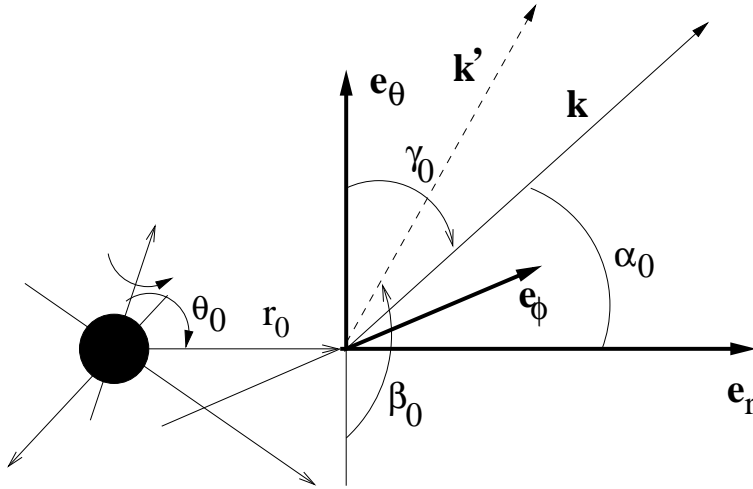


Fig. 6. Definition of directional angles α_0 , β_0 and γ_0 in a local frame. Vectors \mathbf{e}_r , \mathbf{e}_θ , \mathbf{e}_φ are the basic tetrad vectors. Position of the observer (source) is given by the coordinates (r_0, θ_0) . Vector \mathbf{k} represents a photon as observed by the observer in the given tetrad and vector \mathbf{k}' is its projection into the plane $(\mathbf{e}_\theta, \mathbf{e}_\varphi)$.

For each direction of emission in the local frame of a source, there is a corresponding pair of values of the impact parameters λ and \mathcal{L} which can be related to the directional cosines of the photon trajectory in the local frame at the position of the source. Of course, the analysis of the turning points of the radial motion of photons, presented in the previous section, is crucial in determining the local escape

cones as the boundary of the escape cone is given by directional angles related to spherical photon orbits.

Projection of a photon 4-momentum \mathbf{k} onto the local tetrad of an observer is given by the formulae

$$k^{(t)} = -k_{(t)} = 1, \quad (74)$$

$$k^{(r)} = k_{(r)} = \cos \alpha_0, \quad (75)$$

$$k^{(\theta)} = k_{(\theta)} = \sin \alpha_0 \cos \beta_0, \quad (76)$$

$$k^{(\varphi)} = k_{(\varphi)} = \sin \alpha_0 \sin \beta_0, \quad (77)$$

where α_0, β_0 are directional angles of the photon in the local frame (see Figure 6) and $\cos \gamma_0 = \sin \alpha_0 \sin \beta_0$. In terms of the local tetrad components of the photon 4-momentum and the related directional angles, the conserved quantities, namely, the azimuthal momentum Φ , energy E and K read

$$\Phi = k_\varphi = -\omega^{(t)}{}_\varphi k^{(t)} + \omega^{(r)}{}_\varphi k^{(r)} + \omega^{(\theta)}{}_\varphi k^{(\theta)} + \omega^{(\varphi)}{}_\varphi k^{(\varphi)}, \quad (78)$$

$$E = -k_t = \omega^{(t)}{}_t k^{(t)} - \omega^{(r)}{}_t k^{(r)} - \omega^{(\theta)}{}_t k^{(\theta)} - \omega^{(\varphi)}{}_t k^{(\varphi)}, \quad (79)$$

$$K = \frac{1}{\Delta} \{ [E(r^2 + a^2) - a\Phi]^2 - (\Sigma k^r)^2 \}. \quad (80)$$

The impact parameters λ and \mathcal{L} defined by relations (38) and (39) are thus fully determined by any double, D , of angles from the set $M = [\alpha_0, \beta_0, \gamma_0]$.

Having defined the source frame, we can construct light escape cones assuming fixed coordinates of the source r_0, θ_0 . Their construction proceeds in the following steps:

- for given D , say $D = [\alpha_0, \beta_0]$, we calculate $\lambda = \lambda(\alpha_0, \beta_0)$,
- λ determines the behaviour of $\mathcal{L}_{max} = \mathcal{L}_{max}(r; \lambda)$,
- from the analysis presented in the previous section we calculate minimum of \mathcal{L}_{max} , which reads $\mathcal{L}_{max}^{min} = \mathcal{L}_{max}(r_{min}; \lambda)$,
- we search for such a double D which satisfies equation $\mathcal{L}_0(\alpha_0, \beta_0) = \mathcal{L}_{max}(r_{min}; \lambda)$.

Here, we present in detail the construction of light escape cones in particular case of the *L NRF*. The procedure is analogous for the other stationary frames and simply modified for the free-falling frames, being radius dependent.

The impact parameter λ expressed in terms of the angle γ_0 , related to the *L NRF*, reads

$$\lambda_0 = \frac{1}{\Omega_{L NRF 0} + \frac{\Sigma_0 \sqrt{\Delta_0}}{A_0 \sin \theta_0 \cos \gamma_0}}, \quad (81)$$

where index '0' refers to the frame with coordinates $[r_0, \theta_0]$. The minimum of \mathcal{L}_{max} is located at

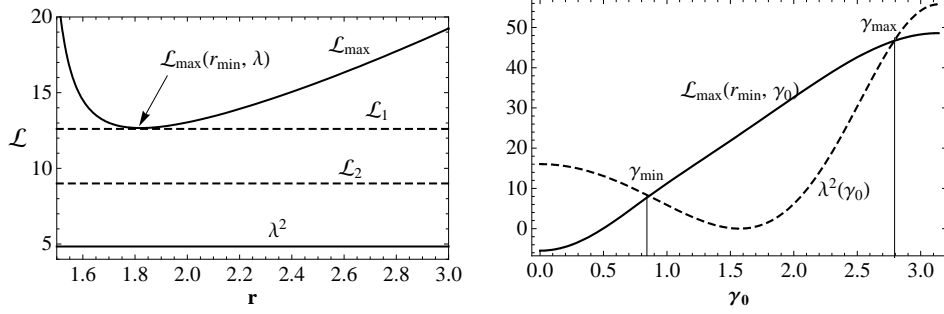


Fig. 7. Left. The functions \mathcal{L}_{max} and $\mathcal{L}_{min} = \lambda_0^2$ are plotted together with representative constant functions \mathcal{L}_1 and \mathcal{L}_2 to demonstrate the construction of the photon escape cone. Right. The intersections of $\mathcal{L}_{max}(\gamma_0)$ with $\lambda^2(\gamma_0)$ give the interval of relevant values of $\gamma_0 \in [\gamma_{min}; \gamma_{max}]$.

$$r_{min} = \begin{cases} \sqrt{a\lambda - a^2} & \text{for } \lambda \geq \lambda_G = a \\ 1 - \frac{k_1}{k_2} + \frac{k_2}{3} & \text{for } \lambda < \lambda_G = a \end{cases} \quad (82)$$

where

$$k_1 = a^2 + 2b + a\lambda - 3, \quad (83)$$

$$k_2 = \left\{ 27(1 - a^2 - b) + 2\sqrt{3}\sqrt{27(1 - a^2 - b)^2 + k_1^3} \right\}^{1/3}. \quad (84)$$

The relevant values of \mathcal{L} lie between \mathcal{L}_{max} and \mathcal{L}_{min} determined by Eqs (41) and (42). The intersections of functions $\mathcal{L}_{max} = \mathcal{L}_{max}(\gamma_0)$ and $\mathcal{L}_{min}(\gamma_0)$ give the relevant interval of angles $\gamma \in [\gamma_{min}, \gamma_{max}]$ (see Figure 7). For each γ from $[\gamma_{min}, \gamma_{max}]$ we calculate minimal value of the photon impact parameter \mathcal{L} for which the photon reaches the turning point r_{min} and escapes to infinity. This minimal value is the minimum of \mathcal{L}_{max} which is located at r_{min} , eg. $\mathcal{L}_{max} = \mathcal{L}_{max}(r_{min}; \lambda_0(\gamma_0), a, b)$, where r_{min} is given by (82). Now we can calculate the value of α_0 using equation

$$\cos \alpha_0 = \frac{k^{(r)}}{k^{(t)}} = \frac{\omega_{LNRF\mu}^{(r)} k^\mu}{\omega_{LNRF\mu}^{(t)} k^\mu}. \quad (85)$$

We arrive to the formula

$$\cos \alpha_0 = \pm \sqrt{A_0} \frac{\sqrt{(r_0^2 + a^2 - a\lambda_0)^2 - \Delta_0(\mathcal{L}_{max}^{min} - 2a\lambda_0 + a^2)}}{-a(a \sin^2 \theta_0 - \lambda_0)\Delta_0 + (r_0^2 + a^2)(r_0^2 + a^2 - a\lambda_0)}, \quad (86)$$

where $A_0 = A(r_0, \theta_0)$, $\Delta_0 = \Delta(r_0)$ and $\mathcal{L}_{max}^{min} = \mathcal{L}_{max}(r_{min}; \lambda_0, a, b)$. The angle β_0 can be calculated from the formula (77). In this way we obtain angles from the arc $\beta_0 \in \langle -\pi/2; \pi/2 \rangle$. The remaining arc $\beta_0 \in \langle \pi/2; 3\pi/2 \rangle$ can be obtained by turning the arc $\beta_0 \in \langle -\pi/2; \pi/2 \rangle$ around the symmetry axis determined by angles

$\beta_0 = -\pi/2$ and $\beta_0 = \pi/2$. This procedure can be done because photons released under angles β_0 and $\pi - \beta_0$ have the same constants of motion. Clearly, for sources under the radius corresponding to the corotating equatorial photon circular orbit, only outward directed photons with no turning point of the r -motion can escape. With radius of the source approaching the event horizon ($r_0 \rightarrow r_+$), the escape cone shrinks to infinitesimal extension, except the case of extreme black hole⁶. For the other frames considered here, the procedure of the related light escape cone construction can be directly repeated, but with the relevant tetrad 1-form components being used in the procedure.

In order to reflect properly the effect of the tidal charge b on the escape cone structure, we shall give the cones for black hole sequences of two kind: first we keep the spin a fixed and change b , second we keep fixed "distance" to the extreme black hole states, i.e., $a^2 + b$ is fixed, and both a and b are changed. The positive tidal charges have tendency to slightly increase the asymmetry of the cones as compared with $b = 0$ case, keeping its character similar to the case of Kerr black holes (see next section). Therefore, we focus our attention to the influence of negative tidal charges.

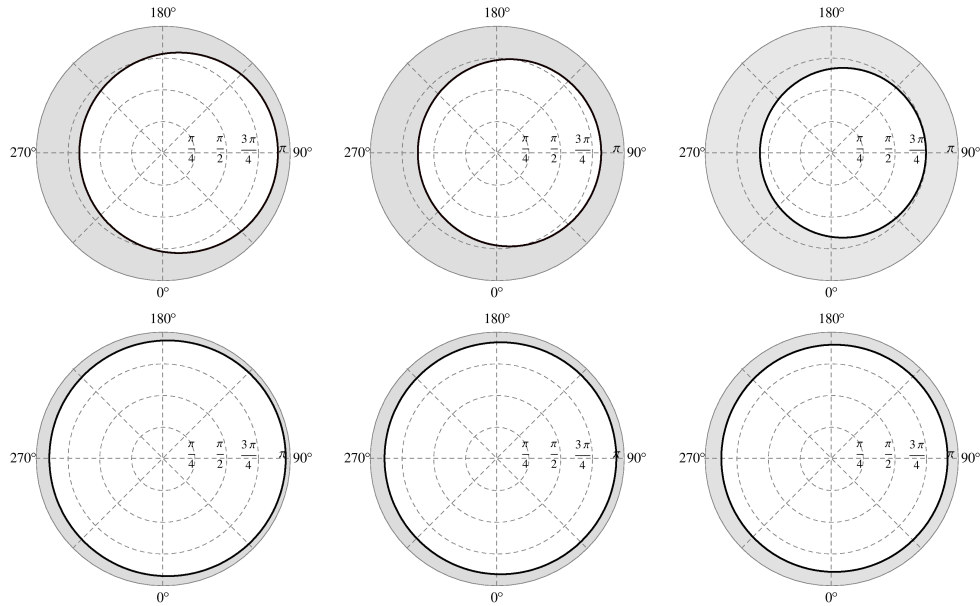


Fig. 8. Light escape cones as seen by *LNRF* in the vicinity of the braneworld Kerr black hole. Top set of images is plotted for radial coordinate of emitter $r_e = 6M$ and bottom set for $r_e = 20M$. The rotational parameter $a = 0.9981$ is fixed and the representative values of the braneworld parameter b are 0 (left), -1 (middle) and -3 (right). The shaded area represents photons captured by black hole.

Behaviour of the *LNRF* escape cones in dependence on the braneworld paramete-

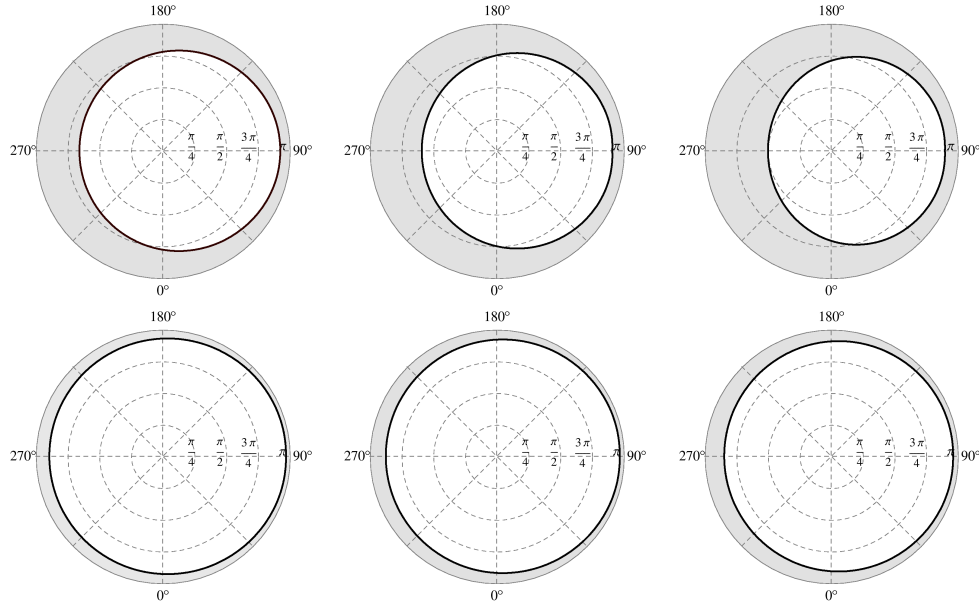


Fig. 9. Light escape cones as seen by *L NRF* in the vicinity of the extreme braneworld Kerr black hole. Top set of images is plotted for radial coordinate of emitter $r_e = 6M$ and bottom set for $r_e = 20M$. The representative rotational and braneworld parameters $[a^2, b]$ are $[1.0, 0.0]$ (left), $[2.0, -1.0]$ (middle) and $[4.0, -3.0]$ (right). The shaded area represents photons captured by black hole.

ter b (and the spin a) is represented in Figures 8 and 9. The complementary trapped cones, corresponding to photons captured by the black hole, are shaded.

At a fixed radius expressed in units of M the extension of the trapped cone grows with descending of b to higher negative values and fixed spin a and mass M , demonstrating thus the growing gravitational pull of the black hole due to growing magnitude of the negative braneworld parameter. The same statement holds also in the case of extreme Kerr black holes, when a grows and b descends, while M is fixed. Clearly, the positive braneworld parameters have tendency to increase the asymmetry of the cones, while the negative ones symmetrize the escape cones with growing of $|b|$. On the other hand, the asymmetry of the escape cone grows with descending of b for extreme black holes (Figure 9).

Table 1. Table of relevant values of r_{ms} and r_h used in plots on Figs 10 and 11.

(a^2, b)	(0.9981, 0.0)	(0.9981, -1.0)	(0.9981, -3.0)
r_{ms}	1.24M	3.91M	6.27M
r_h	1.062M	2.002M	2.73M

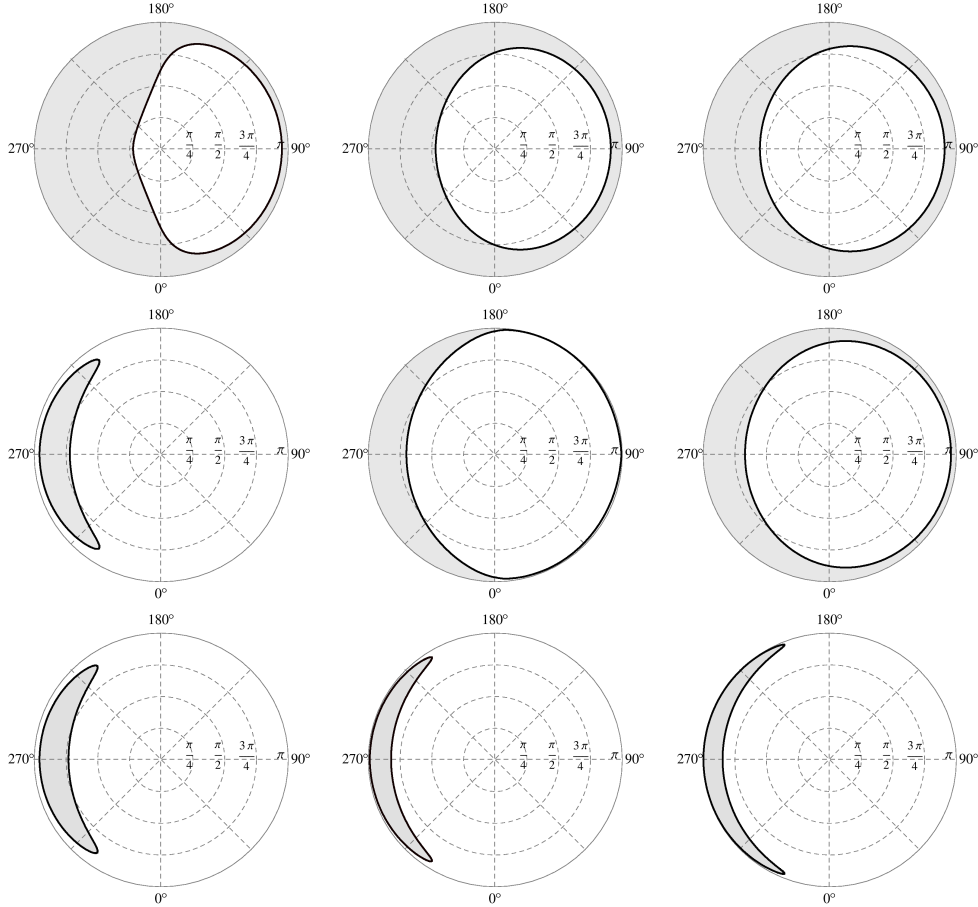


Fig. 10. Escape cones of GF+ observers. Top images are plotted for observer (emitter) at $r = r_{ms}$, middle images $r = 10M$ and bottom images for $r = 10 \cdot r_h$. The value of $a = 0.9981$ is kept fixed. The representative values of b are (from left to right) 0.0, -1.0 and -3 .

Further, we represent the influence of the braneworld parameter on the escape cones for the circular (corotating) geodesic frames in Figure 10. Assuming astrophysically relevant sources in Keplerian accretion discs, their orbits must be located above the marginally stable orbit r_{ms} , determined implicitly by the condition ^{1,45}

$$a = a_{ms}(r; b) \equiv \frac{4(r - b)^{3/2} \mp r\sqrt{3r^2 - 2r(1 + 2b) + 3b}}{3r - 4b}. \quad (87)$$

Therefore, we construct the escape cones for observers at $r = r_{ms}(a, b)$ and at fixed radii. In the sequence of black holes with fixed spin $a = 0.9981$ (Figure 10) we include also a subsequence of escape cones constructed at the same relative distance from the black hole horizon in order to better illustrate the role of the tidal charge b . In the sequence of near-extreme black holes with $a^2 + b = 0.9999$ (Figure 11) the third

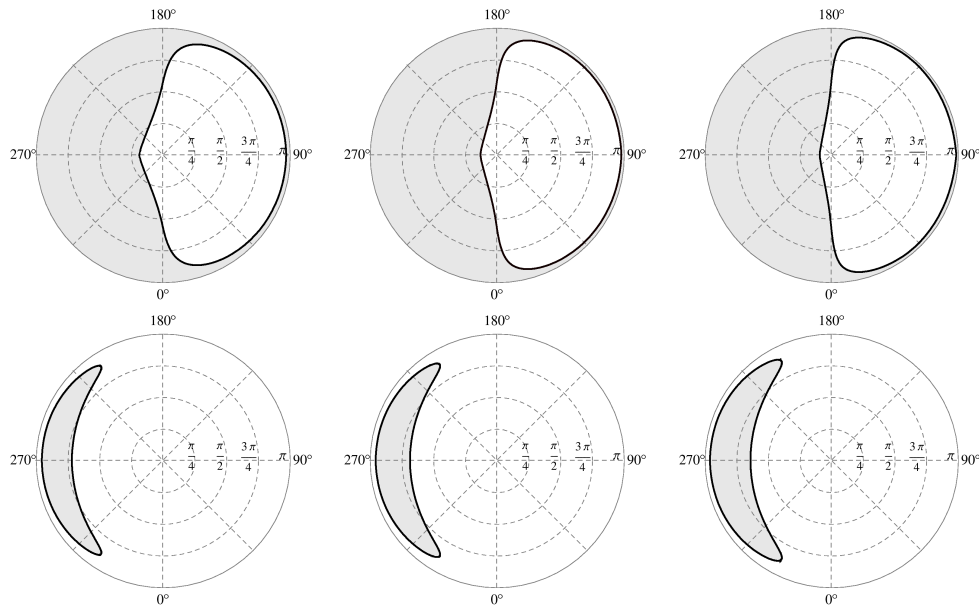


Fig. 11. Escape cones of GF+ observers. Top images are plotted for observer (emitter) at $r = r_{ms}$ and bottom images for $r = 10M$. The value of $a^2 + b = 0.9999$ is kept fixed. The representative values of $(a^2; b)$ are (from left to right) $(0.9999; 0.0)$, $(1.9999; -1.0)$ and $(3.9999; -3)$.

sequence is not necessary as the black hole horizon is fixed at $r_h = 1.01M$. Figures 10 and 11 demonstrate that the trapped cone expands as the tidal charge descends to lower negative values, both for black holes with fixed spin a and for near-extreme holes. On the other hand, considering the cones at r_{ms} we can conclude that the descending tidal charge ($b < 0$) symmetrizes their shape for fixed a , but makes them strongly asymmetric for near-extreme black holes shrinking them strongly in the direction of the black hole rotation.

Finally we demonstrate the relevance of the tidal charge b in the character of escape cones of the RFF_- (comparing them with those related to $L NRF$) in Figure 12. We construct the escape cones for two typical values of the tidal charge ($b = 0$, $b = -3$) in a sequence of radii where the free-falling source is radiating, demonstrating thus the combined growing influence of the black hole gravitational pull on the photon motion and the velocity of the free-falling source. In order to illustrate the phenomena in a clear way, we compare the RFF_- escape cones to the corresponding $L NRF$ escape cones. Clearly, the tidal charge descending to higher negative values makes stronger squeezing of the free-falling cones relative to the $L NRF$ escape cones at any fixed radius. Notice that both the RFF_- and $L NRF$ cones are shifted due to the black hole rotational dragging. We again observe the tendency of negative brany parameters to symmetrize and squeeze the escape cones. At a fixed r , the escape cones become smaller for growing $|b|$ due to stronger gravity. For completeness we present sequence of both the RFF_- and $L NRF$ escape cones

at the three fixed radii for an extreme black hole with $b = -3$ and $a^2 = 4$. We observe that both the RFF_- and LNR cones are strongly shifted in the sense of the black hole rotation in vicinity of black hole horizon due to growing influence of the spin. The symmetrizing effect of descending values of negative tidal charge is canceled by strong influence of the rotational effects due to growing black hole spin.

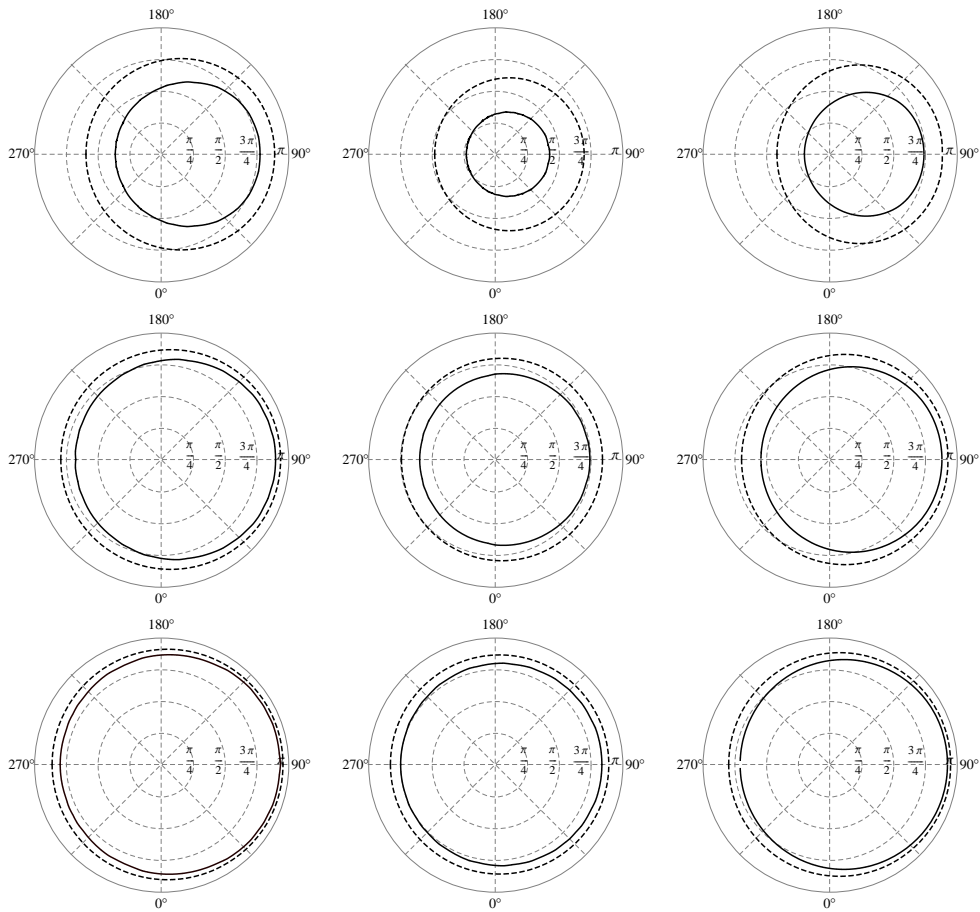


Fig. 12. Comparison of the effect of the tidal charge b on the shape of light escape cones of locally nonrotating (dashed curves) frames and free falling (solid curves) frames. In the left column light escape cones are plotted for the tidal charge parameter $b = 0$ and in the middle one the light escape cones are plotted for $b = -3$. The spin $a = 0.9981$ is kept fixed in both columns. The right column gives the sequence of the escape cones for an extreme black hole with $[a^2 = 4; b = -3]$. Emitting sources in all plots are moving in the equatorial plane. The radial distances of emitter are $r_e = 5M$ (top row), $r_e = 10M$ (middle row) and $r_e = 15M$ (bottom row).

5. Silhouette of braneworld Kerr black hole

In principle, it is of astrophysical importance to consider a black hole in front of a source of illumination whose angular size is large compared with the angular size of the black hole⁶. A distant observer will see a silhouette of the black hole, i.e., a black hole in the larger bright source. The rim of the black hole silhouette corresponds to photon trajectories spiralling around the black hole many times before they reach the observer. Of course, the shape of the silhouette enables, in principle, determination of the black hole parameters. But we have to be aware of the strong dependency of the silhouette shape on the observer viewing angle; clearly, the shape will be circular for observers on the black hole rotation axis, and its deformation grows with observer approaching the equatorial plane.

Assuming that distant observers measure photon directions relative to the symmetry center of the gravitational field, the component of the angular displacement perpendicular to the symmetry axis is given by $-p^{(\varphi)}/p^{(t)}$ (for black hole rotating anticlockwise relative to distant observers), while for angular displacement parallel to the axis it is given by $p^{(\theta)}/p^{(t)}$. These angles are proportional to $1/r_0$, therefore, it is convenient to use the impact parameters in the form independent of r_0 ⁶

$$\tilde{\alpha} = -r_0 \frac{p^{(\varphi)}}{p^{(t)}} = -\frac{\lambda}{\sin \theta_0}, \quad (88)$$

and

$$\begin{aligned} \tilde{\beta} &= r_0 \frac{p^{(\theta)}}{p^{(t)}} = [q + a^2 \cos^2 \theta_0 - \lambda^2 \cot^2 \theta_0]^{1/2} \\ &= \left[\mathcal{L} + a^2 \cos^2 \theta - \frac{\lambda^2}{\sin^2 \theta_0} \right]^{1/2}. \end{aligned} \quad (89)$$

Photon trajectories reaching the observer are represented by points in the $(\tilde{\alpha} - \tilde{\beta})$ plane representing a small portion of the celestial sphere of the observer.

The shape of the black hole silhouette is the boundary of the no-turning-point region, i.e., it is the curve $\mathcal{L} = \mathcal{L}_{max}^{min}(\lambda)$ expressed in the $(\tilde{\alpha} - \tilde{\beta})$ plane of the impact parameters. For observers in the equatorial plane ($\theta_0 = \pi/2$), $\tilde{\alpha} = -\lambda$, $\tilde{\beta} = (\mathcal{L} - \lambda^2)^{1/2} = q^{1/2}$.

We consider that the black hole is observed by static distant observers. Therefore, we shall use the static frames introduced above. The silhouette of the black hole is quite naturally related to their trapped (escape) light cones.

The marginal values of impact parameters λ_0 and \mathcal{L}_0 (resp q_0) are obtained from the light escape cone. Using the stationarity of the braneworld Kerr spacetime we “shoot out“ virtual photons from observer (static frame at very large distance r_0) and we are looking for the light escape cone of this virtual source (using the results of the previous section). The trapped light cone of this virtual source is constructed from the light escape cone of the virtual source by transformations of directional

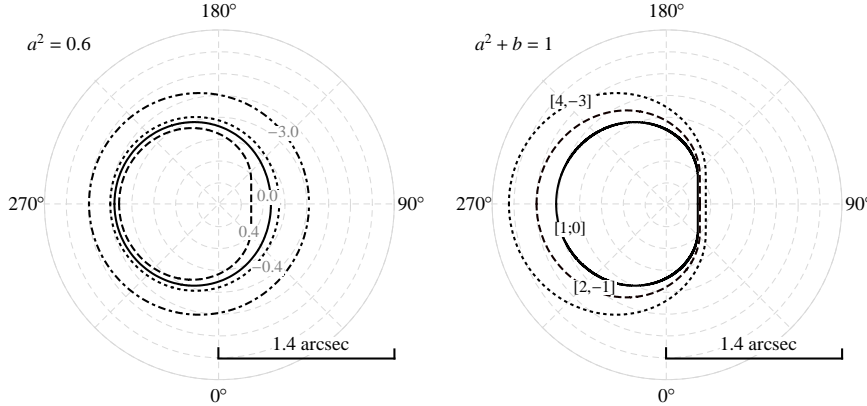


Fig. 13. Left figure. The $(\bar{\alpha}_0, \bar{\beta}_0)$ plots of the silhouettes of braneworld Kerr black hole on a bright background for rotational parameter $a^2 = 0.6$ and four representative values of tidal charge parameter $b = -3.0$, $b = -0.4$, $b = 0.0$ and $b = 0.4$. The observer is located at $r_0 = 10^4 M$ and $\theta_0 = 90^\circ$. Right figure. The silhouettes of extreme black holes for three representative values of braneworld parameter $b = 0$ (solid), $b = -1$ (dashed) and $b = -3$ (dotted). Static observer is in equatorial plane at radial distance from the centre $r_0 = 10^4 M$.

angle α_0 to $\bar{\alpha}_0 = \pi - \alpha_0$ and directional angle β_0 to $\bar{\beta}_0 = \beta_0$. In this way we get marginal directions for received photons from bright background behind the black hole. Then we can use the formulas (78), (79) and (80) to calculate the marginal values of λ_0 and $q_0(\mathcal{L}_0)$ in order to obtain the silhouette of the braneworld Kerr black hole in the plane $(\bar{\alpha} - \bar{\beta})$, i.e., the set of doubles $(\bar{\alpha}_0, \bar{\beta}_0)$ from equations (88) and (89). Here we plotted the silhouette directly from the trapped light cone $(\bar{\alpha}_0, \bar{\beta}_0)$ on the observer's sky $(\bar{\alpha}_0 \sin \bar{\beta}_0, \bar{\alpha}_0 \cos \bar{\beta}_0)$. Note that the angle $\bar{\alpha}_0$ is the radial coordinate and the angle $\bar{\beta}_0$ is the polar coordinate in the polar graph of the silhouette.

We shall give the silhouette of the black hole for observers located at fixed radius $r_0 = 10^4 M$ that corresponds to the angular size of $\alpha \sim 1.4 \text{ arcsec}$; for higher distances the angular size falls accordingly to the $1/r_0$ dependence.

First, we give an illustrative picture of the tidal charge influence on the silhouette properties for maximal inclination angle $\theta_0 = 90^\circ$ when the black hole rotational effects are strongest (Figure 13). We present a sequence of silhouettes for fixed black hole spin and varying b (left) and for extreme black holes with $a^2 + b = 1$ and both a, b varying (right). We clearly see that the positive tidal charge squeezes magnitude of the silhouette making its shape more asymmetric, while negative tidal charge enlarges silhouette's diameter symmetrizing its shape when a is fixed. For extreme black holes the silhouette asymmetry is kept but its extension grows with b descending to higher negative values.

Second, there is a crucial effect of the viewing angle θ_0 onto the shape of the black hole silhouette, demonstrated in Figure 14 for representative values of b and fixed spin a , and in Figure 15 for extreme black holes with parameters $[a^2 = 1; b = 0]$

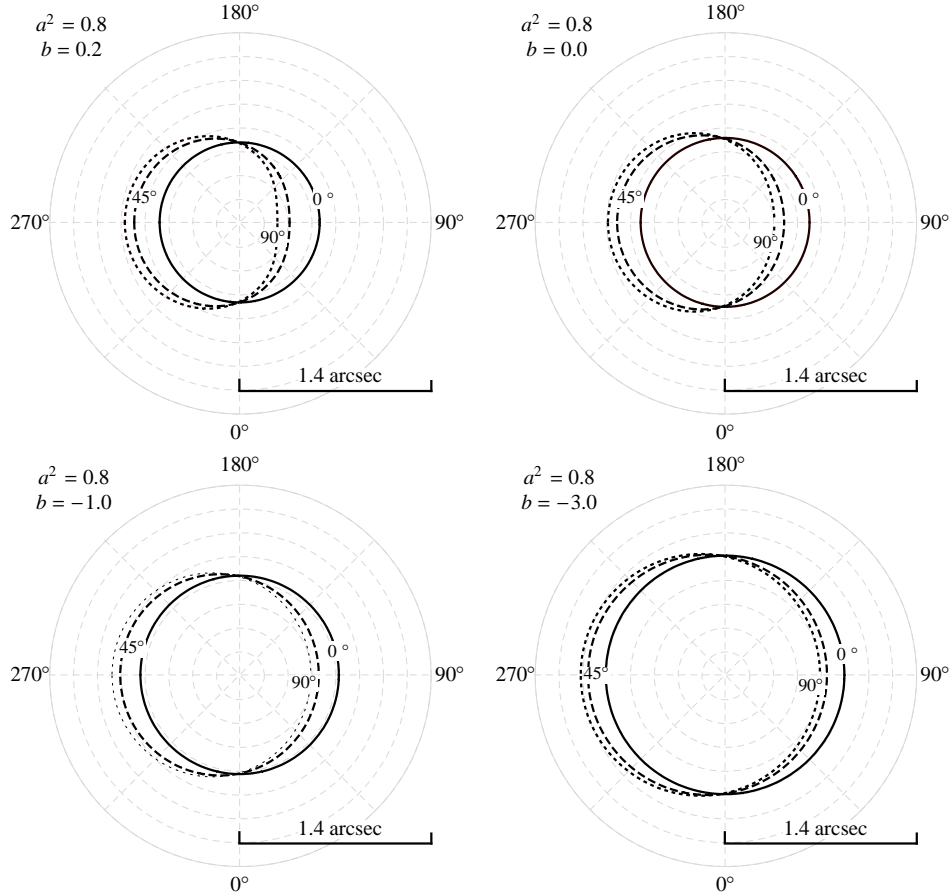


Fig. 14. The silhouettes of rotating braneworld black hole on a bright background. Each image contains three black hole shapes for three representative values of observer's inclination angle $\theta_0 = \{0^\circ (\text{solid}), 45^\circ (\text{dashed}), 90^\circ (\text{dotted})\}$, observer's radial coordinate $r_0 = 10^4 M$ and the rotational parameter $a^2 = 0.8$. Top left image: $b = 0.2$. Top right image: $b = 0.0$. Bottom left image: $b = -1.0$. Bottom right image: $b = -3.0$.

and $[a^2 = 4; b = -3]$.

The rotational effect on the shape of the silhouette grows with inclination angle growing and becomes strongest when $\theta_0 = \pi/2$; then the suppressing effect of the braneworld parameter is given in the most explicit form as demonstrated in Figure 13.

The negative values of the braneworld parameter have the tendency to make the silhouette of a Kerr black hole (with a^2 fixed and for r_0, θ_0 fixed) spherical, suppressing thus the rotational effects. However the symmetrizing effect of the tidal charge could be masked by symmetrizing effect of the viewing angle θ_0 . Therefore, it is very important for black hole parameter estimates to have observational limits on the value of θ_0 .

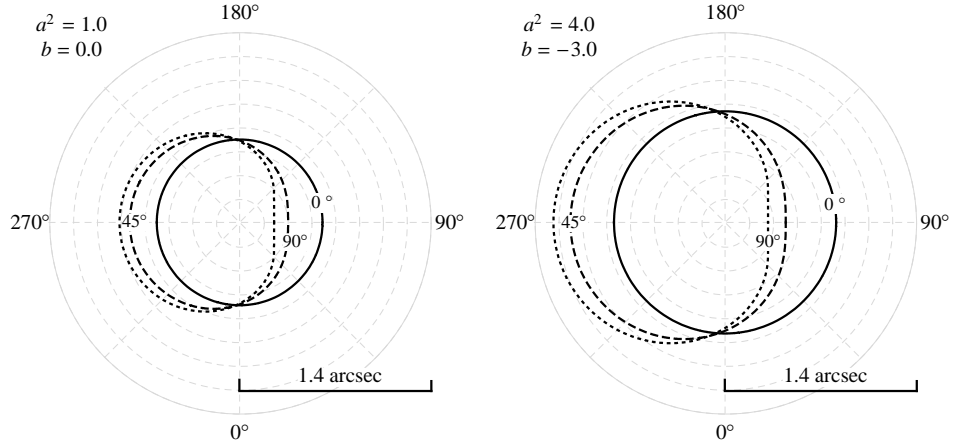


Fig. 15. The silhouettes of extreme rotating braneworld black holes on a bright background. Each image contains three black hole shapes for three representative values of observer's inclination angle $\theta_0 = \{0^\circ \text{ (solid)}, 45^\circ \text{ (dashed)}, 90^\circ \text{ (dotted)}\}$, observer's radial coordinate $r_0 = 10^4 M$. Silhouettes on the left figure are plotted for extreme black holes with $a^2 = 1$ and $b = 0$ and on the right side for $a^2 = 4$ and $b = -3$.

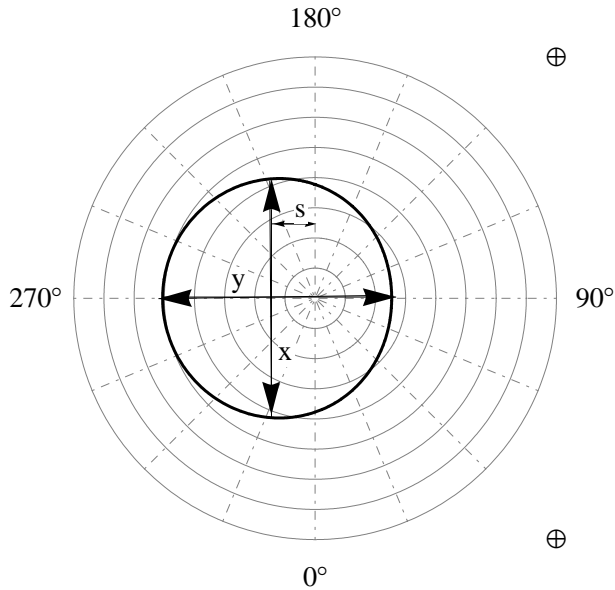


Fig. 16. We define shift s and ellipticity $\epsilon = x/y$ as parameters enabling us to characterize the magnitude of distortion of Kerr black hole silhouette in braneworld universe.

In order to characterize the influence of the tidal charge on the silhouette of a Kerr black hole we define two quantities in principle measurable by distant observers. The

28 *Jan Schee and Zdeněk Stuchlík*

shift s of the silhouette

$$s = \tilde{\alpha}(\beta_m) \sin(\beta_m - \pi), \quad (90)$$

and its *ellipticity* ϵ

$$\epsilon = \frac{\tilde{\alpha}(\beta = 90^\circ) + \tilde{\alpha}(\beta = 270^\circ)}{2\tilde{\alpha}(\beta_m) \cos(\beta_m - \pi)}, \quad (91)$$

where β_m is defined by $\tilde{\alpha}(\beta_m) \sin(\beta_m - \pi) \geq \tilde{\alpha}(\beta) \sin(\beta - \pi)$, $\forall \beta \in [\pi/2, 3/2\pi]$ i.e., it defines maximal extension of the silhouette in the x -direction. The definition of *shift* s and *ellipticity* ϵ is illustrated in Figure 16.

We calculated shift s and ellipticity ϵ as functions of tidal parameter b for the Kerr black hole with rotational parameter $a^2 = 0.9995$ (see Figure 17). Clearly, these are quantities that could be measured and used for a black hole parameters estimates, if observational techniques could be developed to the level enabling the silhouette detailed measuring. We shall discuss such a possibility for the case of the supermassive black hole predicted in the Galaxy Centre (Sgr A^*).

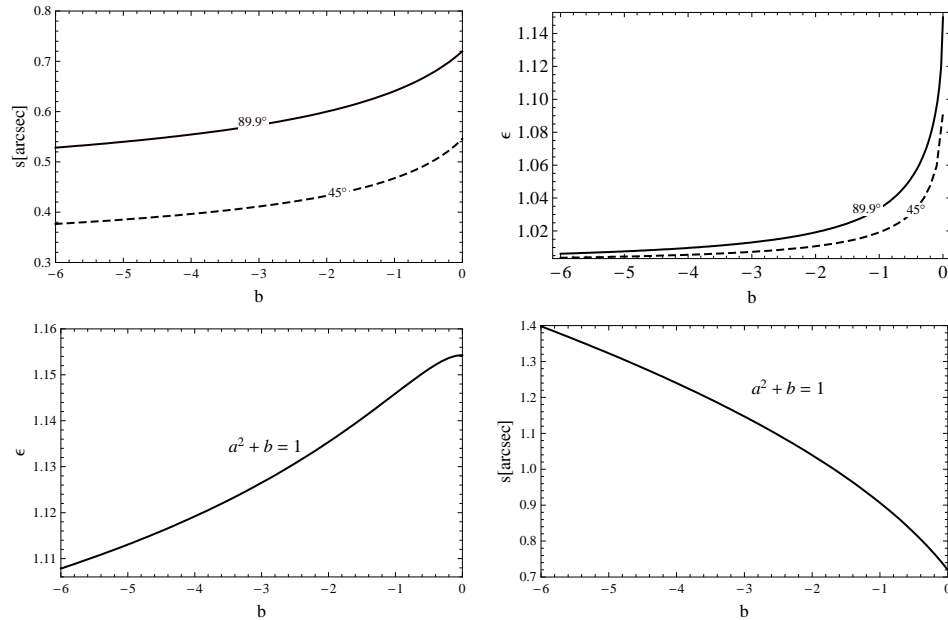


Fig. 17. Top row. Left figure: the shift $s = s(b)$ as a function of braneworld parameter b . Right figure: the ellipticity $\epsilon = \epsilon(b)$ as a function of b . There are two curves on each image, one for observer inclination angle $\theta_0 = 45^\circ$ and second for $\theta_0 = 89.9^\circ$. The rotational parameter of black hole is fixed to value $a = 0.9995$ and the radial coordinate of observer if $r_0 = 10^4 M$. Bottom row. The ellipticity ϵ (left) and shift s (right) of the extreme black hole silhouette as functions of braneworld parameter b . Observer's coordinates are $\theta_0 = \pi/2$ and $r_0 = 10^4 M$.

6. Direct and indirect images of radiating disc

Modelling of spectral line profiles of a thin radiating ring rotating in the equatorial plane of a braneworld Kerr black hole or light curve of an isotropically emitting point source orbiting such a black hole will give us information about the influence of the braneworld parameter b on the optical phenomena in the strong field regime³⁵. Here we restrict our attention to images of radiating discs. We can then, at least in principle, obtain estimates on the astrophysically acceptable values of the braneworld parameter b .

6.1. Images of isoradial geodesics

Calculating images of an accretion disc (ring) in the equatorial plane of a braneworld Kerr black hole is the first step to calculate the optical phenomena. Generally one could obtain a direct and an indirect image (see Figures 18 and 19), but in special cases the situation can be much more complicated due to complex character of the latitudinal and azimuthal photon motion. Here we focus our attention to the direct and indirect images of isoradial geodesics.

In order to find all relevant positions of points forming the rotating ring on observer's sky, we have to find photon trajectories between the ring particles and the observer, i.e., we seek for such doubles of local observational angles $[\alpha_0, \beta_0]$ that satisfy the condition

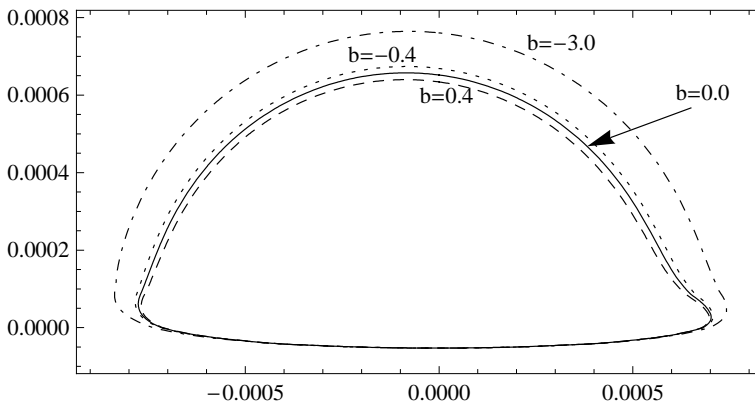


Fig. 18. *Direct image of the rotating ring in the equatorial plane at $r_e = 6M$ around braneworld Kerr black hole with rotational parameter $a^2 = 0.5$ for four representative values of tidal charge parameter $b = -3.0$, $b = -0.4$, $b = 0.0$ and $b = 0.4$. The observer is located at $r_0 = 10^4 M$ and $\theta_0 = 85^\circ$.*

$$I_U(\alpha_0, \beta_0; n_u, u_{sgn}) - I_M(\alpha_0, \beta_0; n, p, s) = 0. \quad (92)$$

Here we introduced the modified radial coordinate $u = 1/r$ and cosine of latitudinal coordinate $\mu = \cos \theta$ ³². In the condition (92) n_u is the number of turning points in u

30 *Jan Schee and Zdeněk Stuchlík*

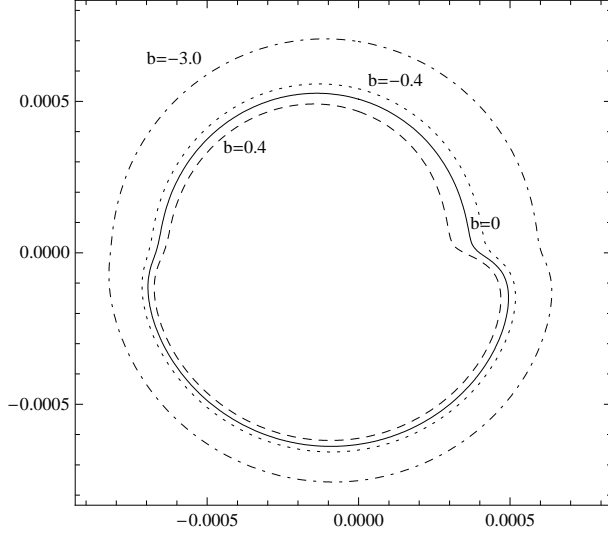


Fig. 19. *Indirect* image of the rotating ring in the equatorial plane at $r_e = 6M$ around braneworld Kerr black hole with rotational parameter $a^2 = 0.5$ for four representative values of tidal charge parameter $b = -3.0$, $b = -0.4$, $b = 0.0$ and $b = 0.4$. The observer is located at $r_0 = 10^4 M$ and $\theta_0 = 85^\circ$.

coordinate, n is the number of turning points passed in μ coordinate, $p = \text{mod}(n, 2)$, $s = (1 - \mu_{sgn})/2$. In terms of u and μ we define the functions I_U and I_M by

$$I_U(\alpha_0, \beta_0; n_u, u_{sgn}) \equiv \begin{cases} -u_{sgn} \left(\int_{u_t}^{u_0} + \int_{u_t}^{u_e} \right) & \text{for } n_u = 1 \\ u_{sgn} \int_{u_0}^{u_e} & \text{for } n_u = 0 \end{cases} \quad (93)$$

and

$$I_M(\alpha_0, \beta_0; n, p, s) \equiv \mu_{sgn} \left[\int_{\mu_0}^{\mu^+} + (-1)^{n+1} \int_{\mu_e}^{\mu^+} + \right. \\ \left. + (-1)^s [(1-p)n + p[(1-s)(n-1) + s(n+1)]] \int_{\mu_-}^{\mu^+} \right] \quad (94)$$

with

$$\int_{u_1}^{u_2} \equiv \int_{u_1}^{u_2} \frac{du}{\sqrt{U(u)}}, \quad (95)$$

$$U(u) = 1 + (a^2 - \lambda^2 - q)u^2 + 2[(\lambda^2 - a^2)^2 + q]u^3 - [q(a^2 + b) + b(a - \lambda)^2]u^4 \quad (96)$$

and

$$\int_{\mu_1}^{\mu_2} \equiv \int_{\mu_1}^{\mu_2} \frac{d\mu}{\sqrt{M(\mu)}}, \quad (97)$$

$$M(\mu) = q + (a^2 - \lambda^2 - q)\mu^2 - a^2\mu^4. \quad (98)$$

6.2. Integration of photon trajectories

We express the integrals (95) and (97) in the form of the standard elliptic integrals of the first kind. Rauch and Blandford presented the tables of reductions of u -integrals and μ -integrals for the case of photons in Kerr geometry³². Here we extended those reductions for the case of nonzero braneworld parameter b . Because the integration of the μ -integral does not depend on braneworld parameter b , the transformations are the same as in the case of Kerr metric³², but we include them for completeness.

There are two cases we distinguish in latitudinal integral (see table 2). In the first case there is one positive, $M_+ > 0$, and one negative, $M_- < 0$ root of $M(m^2)$ it implies that there are two turning points located symmetrically about the equatorial plane given by $\pm\sqrt{M_+}$ (so called orbital motion^{8,13}). In the second case there are two positive roots, $0 < M_- < M_+$ of $M(m^2)$, which implies that the latitudinal motion is constrained to the region above or below of the equatorial plane (so called vortical motion). The relevant reductions of the integral $\int_{m_1}^m dm'/\sqrt{M(m')} = I_M$ are stored in the table 2.

For distant observers we distinguish five relevant cases of the radial integral. These cases depend on the character of roots of the quartic equation $U(u) = 0$, i.e., on the number of turning points ($n_u = 0$ or $n_u = 1$) in the radial motion and the value of parameter $\tilde{q} = q(a^2 + b) + b(a - \lambda)^2$. We have arranged those transformations into table 3.

Denoting roots of the quartic equation $U(u) = 0$ by $\beta_1, \beta_2, \beta_3$ and β_4 , the meaning of each of the five cases is the following:

- The **case I**: four distinct real roots of $U(u) = 0$ forming the sequence $\beta_1 > \beta_2 > \beta_3 > 0$ and $\beta_4 < 0$. The value of modified constant of motion $\tilde{q} > 0$.
- The **case II**: four real roots as in the case I but their values form the following order: $\beta_1 > \beta_2 > 0$ and $\beta_4 < \beta_3 < 0$. The value of modified constant of motion $\tilde{q} < 0$.
- The **case III**: two real and two complex roots of $U(u) = 0$: β_1 being a complex root, $\beta_2 = \bar{\beta}_1$ and $\beta_4 < \beta_3 < 0$. The value of modified constant of motion $\tilde{q} < 0$.
- The **case IV**: only complex roots: $\beta_2 = \bar{\beta}_1$ and $\beta_4 = \bar{\beta}_3$. The value of modified constant of motion $\tilde{q} < 0$.
- The **case V**: two real and two complex roots of $U(u) = 0$: $\beta_1 > 0, \beta_4 < 0, \beta_2$ being a complex root and $\beta_3 = \bar{\beta}_2$.

32 *Jan Schee and Zdeněk Stuchlík*

 Table 2. The reductions of $\int_{m_1}^m dm' / \sqrt{M(m')} = I_M$

Case	$\tan \Psi$	m	c_1	m_1
$M_- < 0$	$\sqrt{\frac{M_+}{m^2} - 1}$	$\frac{M_+}{M_+ - M_-}$	$\frac{1}{\sqrt{a^2(M_+ - M_-)}}$	$\sqrt{M_+}$
$M_- > 0$	$\sqrt{\frac{M_+ - m^2}{m^2 - M_-}}$	$\frac{M_+ - M_-}{M_+}$	$\frac{1}{a^2}$	$\sqrt{M_+}$

 Table 3. The reductions of $\int_{u_1}^u du' / \sqrt{U(u')} = I_U$

Case	$\tan \Psi$	m	c_1	u_1
I	$\sqrt{\frac{(\beta_1 - \beta_3)(u - \beta_4)}{(\beta_1 - \beta_4)(\beta_3 - u)}}$	$\frac{(\beta_1 - \beta_2)(\beta_3 - \beta_4)}{(\beta_1 - \beta_3)(\beta_2 - \beta_4)}$	$\frac{2}{\sqrt{q(b_1 - b_3)(b_2 - b_4)}}$	β_4
II	$\sqrt{\frac{(\beta_1 - \beta_2)(u - \beta_3)}{(\beta_1 - \beta_3)(\beta_2 - u)}}$	$\frac{(\beta_2 - \beta_3)(\beta_1 - \beta_4)}{(\beta_1 - \beta_2)(\beta_4 - \beta_3)}$	$\frac{2}{\sqrt{-q(b_1 - b_2)(b_3 - b_4)}}$	β_3
III	$\frac{2c_2(u)}{ 1 - c_2^2(u) }$	$\frac{4c_4c_5 - (\beta_3 - \beta_4)^2 - c_4c_5}{4c_4c_5}$	$\frac{1}{\sqrt{-q}c_4c_5}$	β_3
IV	$\frac{u - c_3}{\Im(\beta_1)(1 + c_2^2) + c_2(u - c_3)}$	$1 - \left(\frac{c_4 - c_5}{c_4 + c_5}\right)^2$	$\frac{2}{(c_4 + c_5)\sqrt{-q}}$	c_3
V	$\frac{2c_2(u)}{ 1 - c_2^2(u) }$	$1 - \frac{(c_4 + c_5)^2 - (\beta_1 - \beta_4)^2}{4c_4c_5}$	$\frac{1}{\sqrt{q}c_4c_5}$	β_4

Table 4. Definitions for Table 3.

Case	1c_2	1c_3
III	$\left[\frac{c_5(u - \beta_3)}{c_4(u - \beta_4)}\right]^{1/2}$	-
IV	$\left\{\frac{4[\Im(\beta_1)]^2 - (c_4 - c_5)^2}{(c_4 + c_5)^2 - 4[\Im(\beta_1)]^2}\right\}^{1/2}$	$\Re(\beta_1) + c_2\Im(\beta_1)$
V	$\left[\frac{c_4(u - \beta_4)}{c_5(\beta_1 - u)}\right]^{1/2}$	-

Using presented transformations we can write the integrals (95) and (97) in the form

$$\int_{u_1}^u \frac{1}{\sqrt{U(\tilde{u})}} d\tilde{u} = c_1 \mathcal{F}(\Psi; m) \quad (99)$$

and

$$\int_{\mu_1}^{\mu} \frac{1}{\sqrt{M(\tilde{\mu})}} d\tilde{\mu} = c_1 \mathcal{F}(\Psi; m) \quad (100)$$

where \mathcal{F} is the elliptic integral of the first kind and u_1 (resp μ_1) depends on the

Table 5. Definitions for Table 3 and Table 4.

Case	1c_4	1c_5
III	$\left\{[\Re(\beta_1) - \beta_3]^2 + [\Im(\beta_1)]^2\right\}^{1/2}$	$\left\{[\Re(\beta_1) - \beta_4]^2 + [\Im(\beta_1)]^2\right\}^{1/2}$
IV	$\left\{[\Re(\beta_1) - \Re(\beta_3)]^2 + [\Im(\beta_1) + \Im(\beta_3)]^2\right\}^{1/2}$	$\left\{[\Re(\beta_1) - \Re(\beta_3)]^2 + [\Im(\beta_1) - \Im(\beta_3)]^2\right\}^{1/2}$
V	$\left\{[\Re(\beta_2) - \beta_1]^2 + [\Im(\beta_2)]^2\right\}^{1/2}$	$\left\{[\Re(\beta_2) - \beta_4]^2 + [\Im(\beta_2)]^2\right\}^{1/2}$

¹The symbols $\Re(x)$ and $\Im(x)$ refer to real and imaginary part of x here.

case of root distribution of quartic equation $U(u) = 0$ (resp. $M(\mu) = 0$) as given in Table 3 (resp 2). If, in the cases III and V, the value of $1 - c_2^2(u) < 0$, we have to take instead of (99) the form

$$\int_{u_1}^u \frac{1}{\sqrt{U(\tilde{u})}} d\tilde{u} = c_1(2\mathcal{K}(m) - \mathcal{F}(\Psi; m)), \quad (101)$$

where \mathcal{K} is the complete elliptic integral of the first kind. In the case that $\text{sign}(\mu_1 \cdot \mu) < 0$ we have to take instead of (100) the form

$$\int_{\mu_1}^{\mu} \frac{1}{\sqrt{M(\tilde{\mu})}} d\tilde{\mu} = c_1(2\mathcal{K}(m) - \mathcal{F}(\Psi; m)), \quad (102)$$

where Ψ , m and c_1 are taken from table 2. We consider two basic possibilities of trajectories, namely those corresponding to direct and indirect images (Figures 18 and 19).

6.3. Disc images

It is very important to demonstrate the influence of the braneworld parameter on the shape of images of rings in the equatorial plane representing parts of Keplerian accretion discs. Of course, as well known from the Kerr (and even Schwarzschild) black holes, the images strongly depend on the latitude of the observer. We calculate the direct and indirect images of flat discs and combined, full image of the disc for two representative values of viewing angle θ_0 and appropriately chosen extension of radiating disc area.

We include the effect of frequency shift into the calculated images of part of the Keplerian discs assumed to be radiating at a given fixed frequency. The frequency shift g is determined by the ratio of observed (E_0) to emitted (E_e) photon energy

$$g = \frac{E_0}{E_e} = \frac{k_{0\mu} u_0^\mu}{k_{e\mu} u_e^\mu}, \quad (103)$$

where u_0^μ (u_e^μ) are components of the observer (emitter) 4-velocity and $k_{0\mu}$ ($k_{e\mu}$) are components of the photon 4-momentum taken at the moment of emission (observation). For distant observers $u_0^\mu = (1, 0, 0, 0)$. The emitter follows an equatorial

circular geodesics at $r = r_e$, $\theta_e = \pi/2$. Therefore, $u_e^\mu = (u_e^t, 0, 0, u_e^\varphi)$, with components given by

$$u_e^t = \left[1 - \frac{2}{r_e}(1 - a\Omega)^2 - (r_e^2 + a^2)\Omega^2 + \frac{b}{r_e^2}(1 - 2a\Omega) \right]^{-1/2}, \quad (104)$$

$$u_e^\varphi = \Omega u_e^t, \quad (105)$$

where $\Omega = d\varphi/dt$ is the Keplerian angular velocity of the emitter related to distant observers, given by equation (61).

The frequency shift including all relativistic effects is then given by

$$g = \frac{\left[1 - \frac{2}{r_e}(1 - a\Omega)^2 - (r_e^2 + a^2)\Omega^2 + \frac{b}{r_e^2}(1 - 2a\Omega) \right]^{1/2}}{1 - \lambda\Omega} \quad (106)$$

where $\lambda \equiv -k_\varphi/k_t$ is the impact parameter of the photon being a motion constant for an individual photon radiated at a specific position of the radiating disc; notice that g is independent of the second photon motion constant (impact parameter) q . Of course, depending on the position of the emitter along the circular orbit, the impact parameters λ , q of photons reaching a fixed distant observer will vary periodically (see eg., ⁵). For each position of the emitter the impact parameters are determined by the procedure of integration of photon trajectories.

The influence of the frequency shift in the disc images is demonstrated in Figures 20 and 21. The role of the braneworld parameter is illustrated both for small ($\theta_0 = 30^\circ$) and high ($\theta_0 = 80^\circ$) inclination angles. We consider two cases of the radiating disc extension: first one with fixed inner and outer radii, independent of the black hole parameters, and the second one when the inner radius is identified with the marginally stable orbits, depending on the black hole parameters.

In order to map the frequency shift g into color palette we define modified frequency shift $\bar{g} = (g - g_{min})/(g_{max} - g_{min})$ where g_{min} (g_{max}) is the minimal (maximal) value of frequency shift, which is fixed in a particular set of images.

We can see from Figs. 20 and 21 that the negative tidal charge has the tendency to enlarge and symmetrize the disc images.

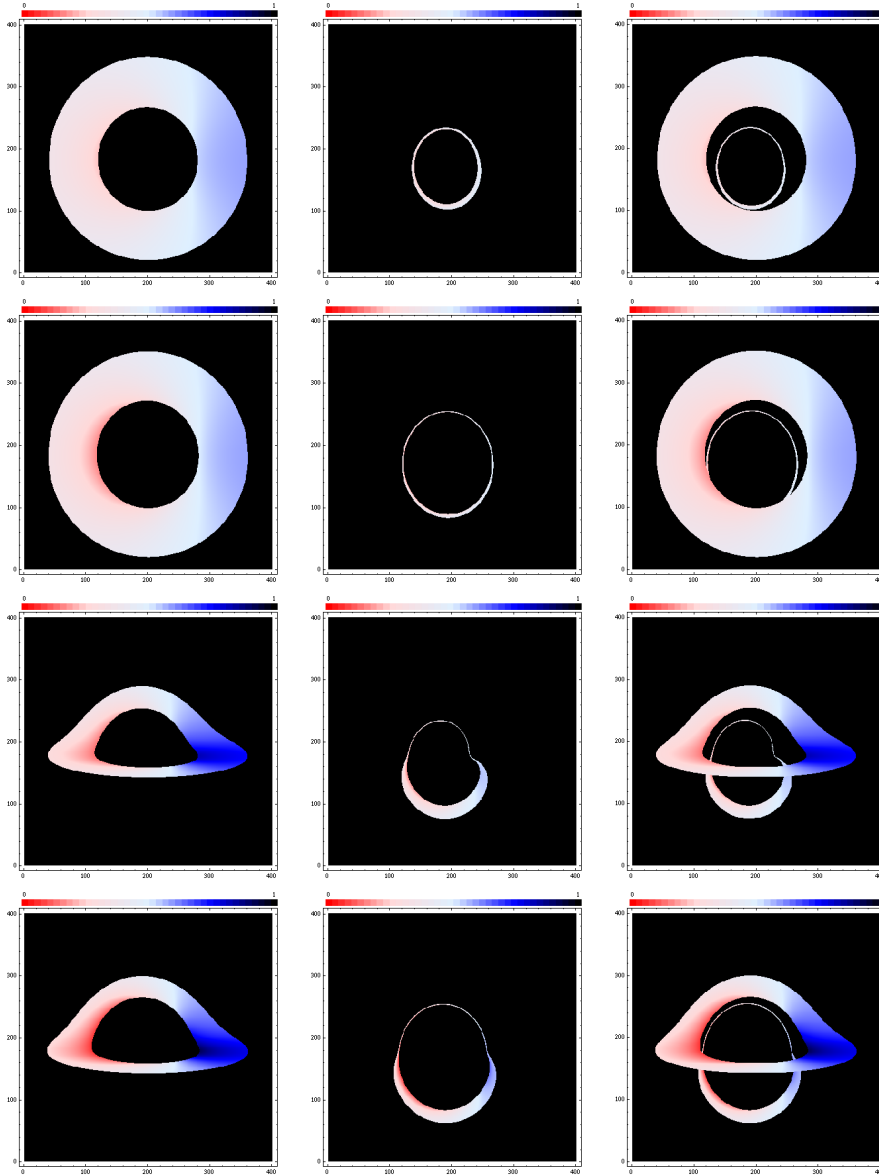


Fig. 20. Radiating Keplerian disc images with fixed inner and outer radii. The modified frequency shift $\bar{g} = (g - g_{min}) / (g_{max} - g_{min})$, with $g_{min} = 0.4$ and $g_{max} = 1.5$, of the radiation emitted from the thin disk with inner radius $r_{in} = 7M$ and outer radius $r_{out} = 15M$, encoded into colors is plotted for representative values of tidal charge parameter $b = -3.0, 0.0$ and inclination of observer $\theta_0 = 30^\circ, 80^\circ$. In the left column direct images are plotted, the indirect images are plotted in the central column and the composition of direct and indirect images is plotted in the right column. The first two rows of images are plotted for the observer inclination $\theta_0 = 30^\circ$ and the second two rows of images are plotted for the observer inclination $\theta_0 = 80^\circ$. Top row images are plotted for $b = 0.0$, the second row images are plotted for $b = -3.0$, the third row images are plotted for $b = 0.0$ and bottom row images are plotted for $b = -3.0$.

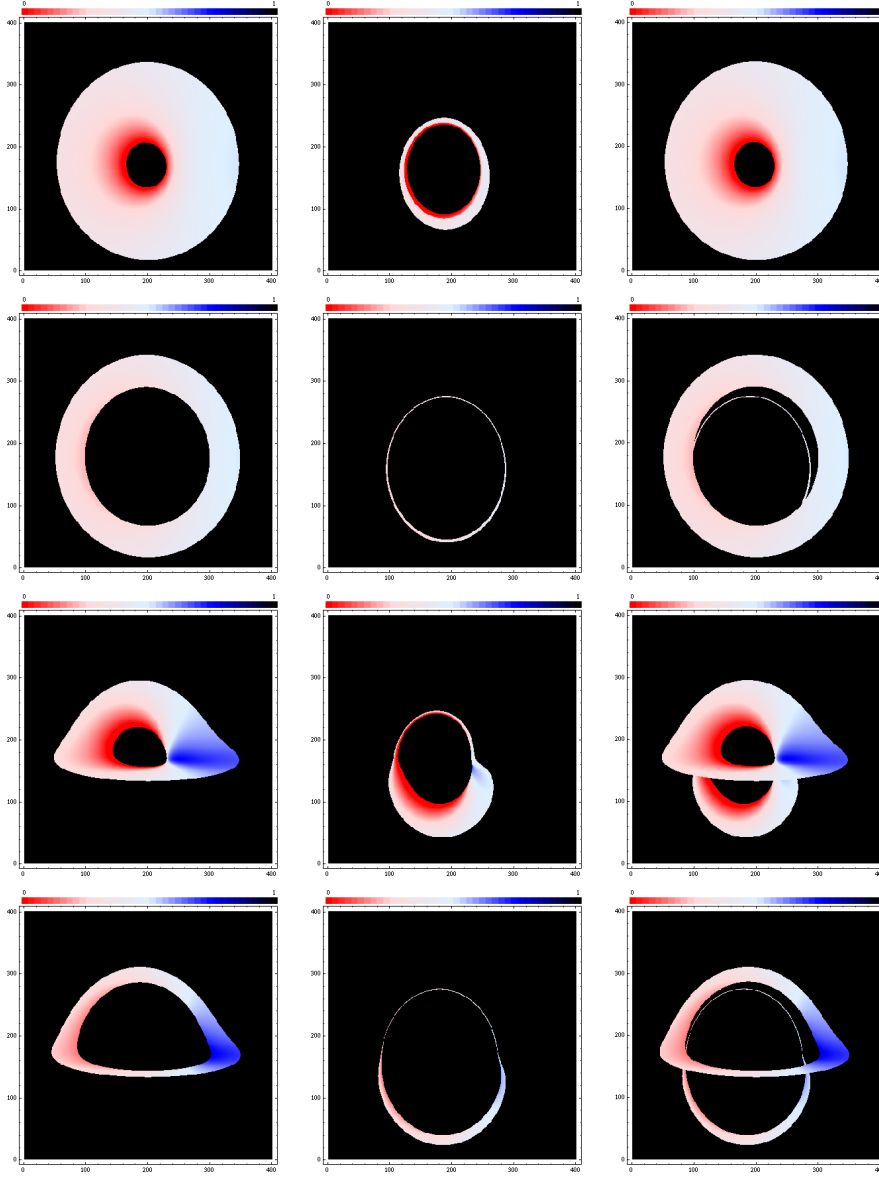


Fig. 21. Radiating Keplerian disc images with $r_{in} = r_{ms}$. The modified frequency shift $\bar{g} = (g - g_{min}) / (g_{max} - g_{min})$, with $g_{min} = 0.2$ and $g_{max} = 1.8$, of the radiation emitted from the thin disk with inner radius $r_{in} = r_{ms}$ (with $r_{ms}(b = 0; a = 0.9981) = 1.3$ and $r_{ms}(b = -3; a = 0.9981) = 6.3$) and outer radius $r_{out} = 10$, encoded into colors is plotted for representative values of tidal charge parameter $b = -3.0, 0.0$ and inclination of observer $\theta_0 = 30^\circ, 80^\circ$. In the left column direct images are plotted, the indirect images are plotted in the central column and the composition of direct and indirect images is plotted in the right column. The first two rows of images are plotted for the observer inclination $\theta_0 = 30^\circ$ and the second two rows of images are plotted for the observer inclination $\theta_0 = 80^\circ$. Top row images are plotted for $b = 0.0$, the second row images are plotted for $b = -3.0$, the third row images are plotted for $b = 0.0$ and bottom row images are plotted for $b = -3.0$.

7. Time delay

For optical effects in vicinity of a black hole, the time delay in case of systems varying with time and observed along two different directions due to the light deflection in strong gravity can be important. The coordinate time that elapses from the instant of photon emission, t_e , to the instant of its reception, t_o , is integrated from the Carter equations and reads

$$t_o = t_e + \mu_{sgn} \int_{\mu_e}^{\mu_o} a^2 \mu^2 \frac{d\mu}{\sqrt{M}} + u_{sgn} \int_{u_e}^{u_o} \frac{2a(a-\lambda)u^3 + a^2u^2 + 1 + ab(\lambda-a)u^4}{(u/u_+ - 1)(u/u_- - 1)\sqrt{U}} du \quad (107)$$

In order to successfully integrate this formula, one must map all the turning points in μ and u motion to correctly set up the signs u_{sgn} and μ_{sgn} .

Suppose that the two light beams, direct and indirect, are emitted at the same coordinate time t_e . They generally reach the observer at different coordinate times t_o^{dir} (t_o^{indir} resp.). By time delay we define here the difference $\Delta t \equiv t_o^{\text{indir}} - t_o^{\text{dir}}$.

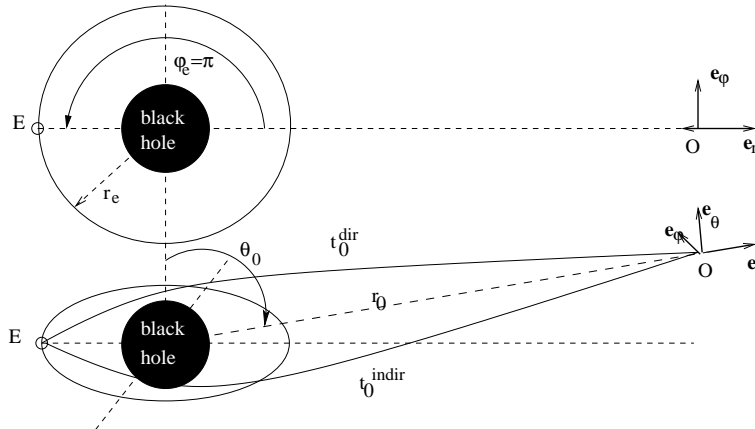


Fig. 22. The illustration of the impact of tidal charge parameter on the time delay Δt in case of direct and indirect photons emitted from emitter E at coordinate time t_e and azimuthal position $\varphi_e = \pi$. They are received at observer O at coordinate times t_o^{dir} (t_o^{indir} resp.). The emitter is on circular geodesic in equatorial plane of braneworld Kerr black hole at radial coordinate $r = r_e$. The observer is far from the center of the black hole at $r = r_o$. Its inclination is $\theta = \theta_o$.

To demonstrate the impact of the tidal charge b on the time delay we consider the following situation (see Figure 22). Let the isotropically radiating monochromatic source orbits in the equatorial plane of the braneworld Kerr black hole at radial distance r_e . It can be switched on and off. When it reaches the azimuthal coordinate $\varphi = \pi$ it is switched on and we compare the coordinate times t_o^{dir} and t_o^{indir} of reception of the photons from the direct and indirect images of the source.

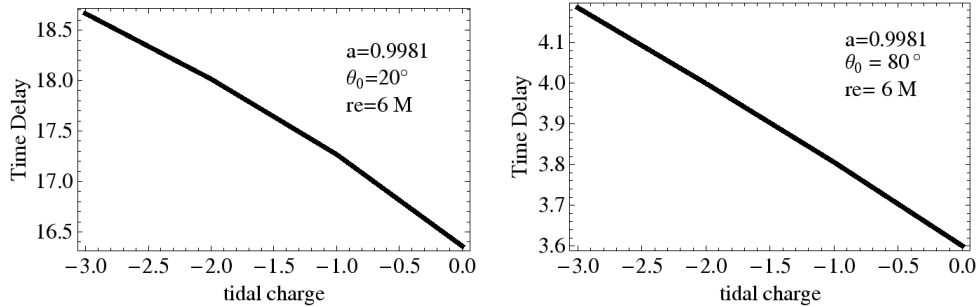


Fig. 23. The difference (“Time Delay“), $\Delta t = t_o^{\text{indir}} - t_o^{\text{dir}}$, between coordinate times of reception of direct and indirect geodesics of photons emitted at the same coordinate time t_e from the azimuthal coordinate $\varphi = \pi$ is plotted as a function of tidal charge b . Left figure: the inclination of the observer is $\theta_0 = 20^\circ$. Right figure: the inclination of the observer is $\theta_0 = 80^\circ$.

The results are demonstrated in the Figure 23. We can directly see that time delay Δt between times of reception of the direct and indirect photons emitted at the same instant from the azimuthal position $\varphi = \pi$ increases as the value of the tidal charge parameter b goes to higher negative values. When b is fixed, the time delay Δt increases as the value of the inclination decreases. The same effects appear for other positions of the radiating spot ($\varphi \neq \pi$). We can see that the time delay Δt depends strongly on the viewing angle θ_0 . Therefore, it is extremely important to have a system with precisely determined viewing angle.

8. Optical phenomena related to Sgr A*

There is an enormously growing evidence that the center of our Galaxy harbors a supermassive black hole whose position could be almost surely identified with the extremely compact radio source Sgr A*. The chain of arguments seems to be very convincing; stars orbiting an unseen mass concentration on elliptical orbits with a common focal position, the unseen mass centered on Sgr A* that seems to be motionless at the dynamical center of the Galaxy, extremely compact emission of the center ³³. Recent measurements of Ghez and collaborators ²⁰ from the W.M. Keck 10 - meter telescopes of a fully unconstrained Keplerian orbit of the short period star SO-2 provide the distance $R_0 = 8.0 \pm 0.6$ kpc and black hole mass $M = (4.1 \pm 0.6) \times 10^6 M_\odot$. If the black hole is assumed to be at rest with respect to the Milky Way Galaxy (i.e., has no massive companion to induce its motion) as argued by Reid ³³, the fit can be further constrained to $R_0 = 8.4 \pm 0.4$ kpc and $M = (4.5 \pm 0.4) \times 10^6 M_\odot$ ²⁰.

Such a close and huge supermassive black hole could be clearly a very convenient object, probably the best one, for testing a wide variety of optical phenomena in strong gravity in its vicinity. The time delay of accidents happening behind the black hole and observed along two directions could be in principle easily measured. We could even expect possibility of black hole silhouette measurements. In this way

the influence of the tidal charge could be properly tested and its value estimated, because for the Galaxy supermassive black hole we can determine relatively precisely the inclination angle of the observer (Solar system), although it is of course very close to $\theta_0 \simeq 90^\circ$.

For non-rotating, Schwarzschild black holes, the silhouette diameter is given by the impact parameter of the photon circular orbit

$$D = 2\lambda_{ph} = 6\sqrt{3}M. \quad (108)$$

Using the Sgr A^* mass estimate $M \sim 4.5 \times 10^6 M_\odot$, we find $D \simeq 55 \mu\text{arcsec}$ while interferometer fringes were reported at wavelength of 1.3 mm and fringe spacing of 0.00005, comparable with the expected value of D . Shorter wavelengths should enable detailed measurements of the black hole silhouette and relatively precise estimates of the black hole parameters due to very precise knowledge of the inclination angle. The angle can be given by the measurement of the Solar system position relative to Galaxy plane $z_\odot \sim 14pc$ ⁴⁹. Then $\theta_0 \sim 89.9^\circ$ or more precisely, θ_0 lies between the values of 89.8772° ($z_\odot = 18pc$) and 89.9318° ($z_\odot = 10pc$). Of course, considering the silhouette shape, it is quite enough to take $\theta_0 = 90^\circ$.

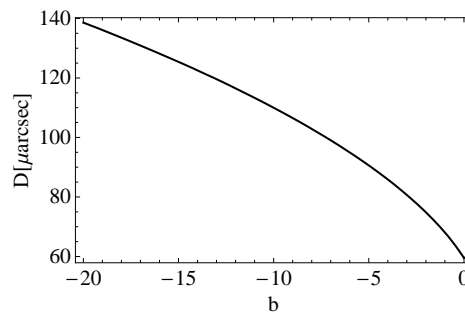


Fig. 24. Diameter D as a function of braneworld parameter b is plotted for Schwarzschild black hole of mass $M = 4.5 \times 10^6 M_\odot$. Observer is at $r_0 = 8.4\text{kpc}$ lying in the equatorial plane.

In the case of spherically symmetric black holes, the influence of the tidal charge parameter b on the silhouette diameter can be given by the simple formula for impact parameter of photon circular orbits that reads⁴⁴

$$\lambda_{ph}(b) = \frac{r_{ph}^2}{\sqrt{r_{ph} - b}} M, \quad (109)$$

where

$$r_{ph}(b) = \frac{3}{2} \left(1 + \sqrt{1 - \frac{8b}{9}} \right). \quad (110)$$

The resulting dependence of the diameter $D(b)$ is illustrated in Figure 24. The diameter grows slowly with the descending of b ; notice that its magnitude is twice the pure Schwarzschild value for $b = -12.8428$. Of course, for rotating black holes the silhouette is maximally deformed due to the influence of rotation since the viewing angle $\theta_0 \sim 90^\circ$ and is given by calculations and results presented above. Testing of the combined spin and tidal charge influence would be possible with measurement precision enlarged for 1-order relative to the recently expected state mentioned above. Clearly, we can expect that the observational accuracy in near future will be high enough to measure the Sgr A^* black hole silhouette implying relevant estimates of the black hole parameters.

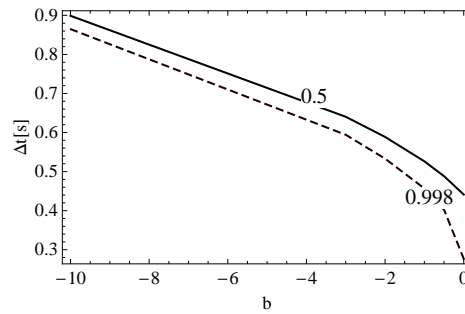


Fig. 25. Comparison of time delay effect as a function of braneworld parameter b between two rotating black holes with rotational parameters $a = 0.5$ and $a = 0.998$. For each b the emitter is radiating from marginally stable orbit. The relevant values of radii r_{ms} of marginally stable orbits are arranged in the Table 6.

Table 6. Table of relevant values of r_{ms} used in plots in Fig 25

b	0.0	-0.5	-1.0	-2.0	-3.0	-10.0
$r_{ms}(a = 0.5)$	4.24M	5.05M	5.73M	6.88M	7.85M	12.88M
$r_{ms}(a = 0.998)$	1.24M	3.03M	3.91M	5.22M	6.28M	11.44M

Considering the time delay effects, the exact value of θ_0 is crucial since it plays a fundamental role in determining the time delay effect whose scale is given by the value of $t \sim 1sec$. We illustrate the influence of the tidal charge on the time delay effects at the astrophysically important radii corresponding to marginally stable circular geodesics, i.e. in the strong gravity regime, for two representative fixed values of black hole spin (see Figure 25 and Table 6). We can expect importance of the regions close to r_{ms} for relevant optical effects due to the idea of the low angular momentum accretion in Sgr A^* advocated by B. Czerny¹¹. Clearly, we can see in Figure 25 that the time delay effects could be well measurable and the tidal charge

influence could be well tested, if the black hole spin is properly estimated.

9. Conclusions

One of the most promising ways of estimating influence of hypothetical hidden external dimensions, considered in the framework of the braneworld model with infinite external dimension as developed by ³¹, seems to be investigation of the optical phenomena caused by the black hole backgrounds. It is so because black holes represent the only case when the non-local influence of the bulk space on the braneworld spacetime structure can be fully described by a single, braneworld parameter called tidal charge, the sign of which can be both positive and negative, with the second possibility being more realistic one ^{1,12}.

Here, we focused our attention to developing a theoretical background for treating the optical phenomena in vicinity of braneworld rotating black holes and bringing general tendencies of the tidal charge effect in some basical optical phenomena.

We have shown qualitatively how the braneworld tidal charge affects the basical optical phenomena, especially the black-hole silhouette, the accretion disc image with the frequency shift of area of the disc radiating at a specific frequency, and the time delay between the direct and indirect images of the hot spot orbiting the black hole. We have shown that these phenomena could be measured and used to put limits on the tidal charge in case of Galaxy Center Sgr A^* supermassive black hole.

We generalized the approaches based on the transfer-function method as introduced and developed in Schwarzschild and Kerr backgrounds ^{16,27,5,42,25,14,17,32} where equations of photon motion are solved in terms of the elliptic integrals (see ^{32,23,24}). For purposes of the present work, the transfer-function method seems to be most efficient. Nevertheless, we prepared the ray-tracing method too, since that could be usefull in treating other optical phenomena.

Generally, rising negative value of the tidal charge strenghtens the black hole field and suppresses the rotational phenomena, when the black-hole rotation parameter is fixed. The magnitude of the optical phenomena grows with decreasing of the negatively-valued tidal charge, but the rotation induced asymmetry of the phenomena like the black-hole silhouette, or the accretion disc image, decreases. The black-hole silhouette is characterized by two parameters, namely the shift of the center and ellipticity, that could be in principle measurable in the Galactic Center black-hole system Sgr A^* , after expected development of observational techniques that at present enable measurement of the black hole diameter, not details of the shape. The Galaxy center (Sgr A^*) seems to be also a promising candidate for testing the time delay effects both for phenomena related to the accretion disc and flares observed there, and for some expected lensing phenomena connected to the observed stars orbiting the Sgr A^* central black hole.

We have found that observable phenomena could be expected for the time-delay effects. Of special interest is comparison of time delays generated for sources in vicinity of the Sgr A^* black hole (both stars and disc hot spots) and those related

to weak lensing of some distant sources^{50,37}.

Similarly, keeping rotational parameter fixed, the negative tidal charge has tendency to make the isoradial curve images (both direct and indirect) larger and less deformed while the positive tidal charge influence is of opposite character. On the other hand, for fixed rotational parameter of the black hole and disc radiating at the innermost part above the innermost stable orbit at $r = r_{ms}$, the negative tidal charge restricts the radiating ring image simply because the radius r_{ms} grows with decreasing value of braneworld parameter b . Suppression of the relativistic effects can be measurable also in the spectral line profiles generated by the inner hot part of the disc radiating at special X-ray line³⁵.

The optical tests have to be confronted with the data obtained from quasiperiodic oscillations observed in some black-hole systems (microquasars³⁴). The orbital resonance model gives good estimates of the black-hole parameters^{48,46,47}; this model has been recently generalized to the case of braneworld Kerr black holes⁴⁵. It is shown that in the case of microquasar GRS 1915+105 and Galactic Center Sgr A* black holes with the negative braneworld parameter b are allowed by the observational data⁴⁵. Detailed modelling of optical phenomena connected to the oscillating discs or orbiting (oscillating) hot spots and related resonant phenomena between the oscillation modes could be very promising in putting limits on allowed values of the tidal charge of the black hole. We plan to elaborate such modelling in future.

Acknowledgements

Research supported by the Czech grant MSM 4781305903 and LC 06014. One of the authors (Zdeněk Stuchlík) would like to express his gratitude to the Czech Committee for Collaboration with CERN for support.

References

1. A. N. Aliev and A. E. Gümrükçüoğlu. Charged rotating black holes on a 3-brane. *Phys. Rev. D*, 71(10):104027–+, 2005.
2. N. Arkani-Hamed, S. Dimopoulos, and G. Dvali. The hierarchy problem and new dimensions at a millimeter. *Phys. Lett. B*, 429:263–272, 1998.
3. B. Aschenbach. Measuring mass and angular momentum of black holes with high-frequency quasi-periodic oscillations. *Astronom. and Astrophys.*, 425:1075–1082, 2004.
4. B. Aschenbach. Measurement of mass and spin of black holes with QPOs. arXiv:0710.3454, 2007.
5. G. Bao and Z. Stuchlík. Accretion disk self-eclipse:x-ray light curve and emission line. *Astrophys. J.*, 400:163–169, 1992.
6. J. M. Bardeen. Timelike and null geodesics in the kerr metric. In *Black holes (Les astres occlus)*, p. 215 - 239, pages 215–239, 1973.
7. J. M. Bardeen, W. H. Press, and S. A. Teukolsky. Rotating black holes: Locally non-rotating frames, energy extraction, and scalar synchrotron radiation. *Astrophys. J.*, 178:347–370, December 1972.

8. J. Bičák and Z. Stuchlík. On the latitudinal and radial motion in the field of a rotating black hole. *Bull. Astron. Inst. Czechosl.*, 27(3), 1976.
9. A. Chamblin, H. S. Reall, H. Shinkai, and T. Shiromizu. Charged brane-world black holes. *Phys. Rev. D*, 63(6):064015, 2001.
10. C. T. Cunningham and J. M. Bardeen. The optical appearance of a star orbiting an extreme kerr black hole. *Astrophys. J.*, 183:237–264, 1973.
11. B. Czerny, M. Mościbrodzka, D. Proga, T. K. Das and A. Siemiginowska. Low angular momentum accretion flow model of Sgr A* activity. In *Proceedings of RAGtime 8/9: Workshops on black holes and neutron stars, Opava, 15–19/19–21 September 2006/2007*, p.35–44, 2007.
12. N. Dadhich, R. Maartens, P. Papadopoulos, and V. Rezanía. Black holes on the brane. *Phys. Lett. B*, 487:1, 2000.
13. F. de Felice and M. Calvani. Orbital and vortical motion in the Kerr metric. *Nuovo Cimento B Serie*, 10:447–458, 1972.
14. M. Dovčiak, V. Karas, G. Matt, and A. Martocchia. Polarization of radiation from AGN accretion discs - the lamp-post model. In S. Hledík and Z. Stuchlík, editors, *RAGtime 6/7: Workshops on black holes and neutron stars*, pages 47–54, December 2005.
15. R. Emparan, M. Masip, and R. Rattazzi. Cosmic rays as probes of large extra dimensions and TeV gravity. *Phys. Rev. D*, 65(6):064023–+, March 2002.
16. A. C. Fabian, M. J. Rees, L. Stella, and N. E. White. X-ray fluorescence from the inner disc in Cygnus X-1. *MNRAS*, 238:729–736, May 1989.
17. C. Fanton, M. Calvani, F. de Felice, and A. Čadež. Detecting accretion disks in active galactic nuclei. *Publ. Astron. Soc. Japan*, (49):159–169, 1997.
18. C. Germani and R. Maartens. Stars in the braneworld. *Phys. Rev. D*, 64:124010, 2001.
19. A. M. Ghez. Stellar orbits and the supermassive black hole at the center of our galaxy. *Am. Astro. Soc.*, 37:531, 2005.
20. A. M. Ghez, S. Salim, N. N. Weinberg, J. R. Lu, T. Do, J. K. Dunn, K. Matthews, M. Morris, S. Yelda, E. E. Becklin, T. Kremenek, M. Milosavljevic, and J. Naiman. Probing the properties of the Milky Way's central supermassive black hole with stellar orbits. *IAU Symposium*, 248, p.52–58, 2008. arXiv:astro-ph 0808.2870
21. V. Karas, D. Vokrouhlicky, and A. G. Polnarev. In the vicinity of a rotating black hole - a fast numerical code for computing observational effects. *MNRAS*, 259:569–575, December 1992.
22. R. P. Kerr. Gravitational field of a spinning mass as an example of algebraically special metrics. *Phys. Rev. Lett.*, (11):26, 1963.
23. G. V. Kraniotis. Frame dragging and bending of light in kerr and kerr (anti) de sitter spacetimes. *Class. and Quant. Grav.*, 22:4391–4424, 2005.
24. G. V. Kraniotis. Periapsis and gravitomagnetic precessions of stellar orbits in kerr and kerr-de sitter black hole spacetimes. *Class. and Quant. Grav.*, 24:1775–1808, 2007.
25. A. Laor. Line profiles from a disk around a rotating black hole. *Astrophys. J.*, 376:90–94, 1991.
26. R. Maartens. Brane-world gravity. *Living Rev. Rel.*, 7:7, 2004.
27. G. Matt, A. C. Fabian, and R. R. Ross. Iron k-alpha lines from x-ray photoionized accretion discs. *MNRAS*, 262:179–186, May 1993.
28. J. E. McClintock, R. Narayan, and R. Shafee. Estimating the spins of stellar-mass black holes. arXiv:0707.4492, 2007. To appear in *Black Holes*, eds. M. Livio and A. Koekemoer (Cambridge University Press), in press (2008).
29. C. W. Misner, K. S. Thorne, and J. A. Wheeler. *Gravitation*. W. H. Freeman and company, San Francisco, 1973.

30. R. Narayan, J. E. McClintock, and R. Shafee. Estimating the spins of stellar-mass black holes by fitting their continuum spectra. arXiv:0710.4073, October 2007.
31. L. Randall and R. Sundrum. An alternative to compactification. *Phys. Rev. Lett.*, 83(23):4690–4693, 1999.
32. K. P. Rauch and R. D. Blandford. Optical caustics in a kerr spacetime and the origin of rapid x-ray variability in active galactic nuclei. *Astrophys. J.*, (421):46–68, 1994.
33. M. J. Reid. Is there a supermassive black hole at the center of the Milky Way? arXiv:0808.2624, 2008
34. R. A. Remillard and J. E. McClintock. X-ray properties of black-hole binaries. *Ann. Rev. of Astron. and Astrophys.*, 44(1):49–92, September 2006.
35. J. Schee and Z. Stuchlík. Spectral line profile in brany kerr spacetime. In *Proceedings of RAGtime 8/9: Workshops on black holes and neutron stars, Opava, 15–19/19–21 September 2006/2007*, p.209–220, 2007.
36. J. Schee, Z. Stuchlík, and J. Juráň. Light escape cones and raytracing in kerr geometry. In *Proceedings of RAGtime 6/7: Workshops on black holes and neutron stars, Opava, 16–18/18–20 September 2004/2005*, p.143–155, 2005.
37. M. Sereno and F. de Luca, "Analytical Kerr black hole lensing in the weak deflection limit", *Phys. Rev. D*, 74, 12, 2006, arXiv:astro-ph/0609435
38. T. Shiromizu, K. Maeda, and M. Sasaki. The einstein equations on the 3-brane world. *Phys. Rev. D*, 62:024012, 2000.
39. T. E. Strohmayer. Raising the curtain on extreme stars. *Astronomy*, 35:32–37, March 2007.
40. Z. Stuchlík. Null geodesics in the kerr-newman metric. *Bull. Astron. Inst. Czechosl.*, 32(6), 1981.
41. Z. Stuchlík. The radial motion of photons in kerr metric. *Bull. Astron. Inst. Czechosl.*, 32(1), 1981.
42. Z. Stuchlík and G. Bao. Radiation from hot spots orbiting an extreme reissner-nordstrm black hole. *General Rel. and Grav.*, 24(9), 1992.
43. Z. Stuchlík, J. Bičák, and V. Balek. The shell of incoherent charged matter falling onto a charged rotation black hole. *Gen. Rel. and Grav.*, 31(53), 1999.
44. Z. Stuchlík and S. Hledík. Properties of the Reissner-Nordstrom spacetimes with a nonzero cosmological constant. *Acta. Phys. Slovaca*, 52, 363, 2002.
45. Z. Stuchlík and A. Kotrlová, "Orbital resonances in discs around braneworld Kerr black holes", *Gen. Rel. and Grav.*, doi: 10.1007/s10714-008-0709-2, 2008, arXiv:0812.5066
46. G. Török. A possible 3:2 orbital epicyclic resonance in qpo frequencies of sgr a*. *Astron. and Astrophys.*, 1(440), 2005a.
47. G. Török. Qpos in microquasars and sgr a* measuring the black hole spin. *Astronom. Nachr.*, 856(326), 2005b.
48. G. Török, M. Abramowicz, W. Kluźniak, and Z. Stuchlík. *Astron. and Astrophys.*, 1(436), 2005.
49. Y. C. Joshi. Displacement of the Sun from the Galactic plane. *MNRAS*, 378:768–776, June 2007. arXiv:astro-ph/0704.0950.
50. A. F. Zakharov. The iron K_{α} -line as a tool for analysis of black hole characteristics. *Publications of the Astronomical Observatory of Belgrade*, 76, 147–162, 2003. arXiv: astro-ph/0411611.